5-2023

Spatial and Statistical Analysis of Groundwater Contaminants in Shallow and Deep Aquifers of the Central Valley of California

Mark G F Nickels
Trinity University, mgf.nickels@gmail.com

SPATIAL AND STATISTICAL ANALYSIS OF GROUNDWATER CONTAMINANTS IN SHALLOW AND DEEP AQUIFERS OF THE CENTRAL VALLEY OF CALIFORNIA

1. Abstract

The sediment aquifer of California's Central Valley is threatened by various contaminants including arsenic (As), iron (Fe), manganese (Mn), and uranium (U). In this region more than six million people and an agricultural industry worth over 20 billion dollars (Faunt et al., 2016) rely predominantly on groundwater, and contamination poses both health risks and financial burdens due to costly remediation. I seek to identify the physical and geochemical processes that mobilize contaminants observed at levels that far exceed both federal and state regulatory standards. Contaminants such as As and U naturally occur in sediment and can be mobilized by either anthropogenic contamination or geogenic changes in the aquifer's geochemistry. I use data from the Groundwater Ambient Monitoring and Assessment (GAMA) program to create spatial, statistical, and geochemical models to elucidate the mobilization mechanisms of As and U. I also explored the stability of aquifer geochemistry as influenced by drought, over-pumping, and agriculture. This study provides evidence that As is strongly correlated with areas of subsidence caused by over-pumping, consistent with the findings of (Smith et al., 2018). As drought conditions in the region worsen, As mobilization will be exacerbated in the shallow aquifer with a lack of oxic recharge causing lower redox potential. U mobilization is more complex and involves a multi-step process. U appears to use NO_3^- as the electron acceptor for oxidation, which oxidatively dissolves U from uraninite in the aquifer matrix. Furthermore, U appears to form aqueous calcium carbonate complexes which prevent its reabsorption onto the mineral surfaces, stabilizing it in groundwater.

2. Introduction

2.1 Geologic Background of the Central Valley

The Central Valley (CV) of California consists of heterogeneous unconsolidated sediments ranging from coarse sand to clay size particles that comprise spatially complex unconfined, confined, and semi-confined aquifers (Faunt et al., 2016, 2009). The CV is comprised of several watersheds that make up two larger hydrogeologic basins: the Sacramento Valley (SV) in the northern CV and the San Joaquin Valley (SJV) in the southern CV. Groundwater in the SV discharges into the Sacramento River and its tributaries, while groundwater in the SJV discharges into the San Joaquin River and its tributaries. Both rivers discharge into the San Francisco Bay (Faunt et al., 2009).

The CV is flanked on the east by the granitic Sierra Nevada range and on the west by the Coastal Range, which was formed by marine deposition (Figure 1) (Faunt et al., 2009). Weathering and erosion from both ranges has produced valley fill consisting of generally sand-size grains that make up groundwater aquifers with interbedded clay lenses that form discontinuous aquitards and aquicludes. Groundwater stored in aquifers is withdrawn throughout the valley for municipal, agricultural, and residential purposes. The major continuous aquitard in the CV is the Corcoran Clay, which bisects the western SJV extending from Bakersfield to Stockton (Faunt et al., 2009; Frink and Kues, 1954; Schmid et al., 2006). This layer consists of fine-grained lacustrine deposits from a Pliocene lake and is 10-200 ft thick. It is generally 50-900 ft below the land surface and is generally deeper to the west (Faunt et al., 2009). The Corcoran Clay acts as the primary confining unit for deep groundwater in the SJV (Frink and Kues, 1954; Nolan and Weber, 2015). Most of the aquifer recharge that feeds both confined and unconfined aquifers in the CV is from snowmelt in the Sierra Nevada delivered via major rivers that originate in the mountains (Figure 1).

Texture Region

Sacramento Valley (SV)
- Redding
- Western Sacramento
- Eastern Sacramento

San Joaquin Valley (SJV)
- Tracy/Delta-Mendota
- Westside
- Northern San Joaquin
- Chowchilla-Madera
- Kings
- Tulare/Kern

California Geologic Map

Generalized Rock Type
- Unconsolidated, Undifferentiated Sediment
- Volcanic and Pyroclastic Flows
- Felsic and Intermediate Igneous Rocks
- Mafic Igneous Rocks
- Ultramafic Rocks
- Metamorphic Rocks
- Siliciclastic and Clastic Rocks
- Carbonates
- Corcoran Clay Extent
- NHD Major Rivers
- Central Valley Outline

N

0   75   150   300 Km

Figure 1. Map of the study site with regional geology, textural region in the top right call out (Faunt et al. 2009) with major rivers from the National Hydrogeologic Database (NHD), and geographic boundaries. The SV consists of Redding, Western and Eastern Sacramento. The SJV consists of all other Textural Regions.

2.2 Water Quantity and Quality

Groundwater in the Central Valley of California has historically served as a primary water source for both major municipalities and a highly productive agricultural industry (Famiglietti et al., 2011; Ghasemizade et al., 2019). Supporting the agriculture industry has required major groundwater withdrawals that have caused consequences such as land subsidence (Faunt et al., 2016), losing streams (Fleckenstein et al., 2004), dried-up wells, and increased pumping costs (Nelson et al., 2016). Furthermore, the CV has experienced several prolonged droughts recently (for example, 2020-2023, 2011-2019, and 2007-2010). Combined, groundwater withdrawals and prolonged droughts are expected to lower water levels and exacerbate subsidence, loss of aquifer storage, and the drying up of shallower wells (He et al., 2017).

Recently, drought periods end in an abnormally wet winter with the melting snowpack and rain recharging the aquifers. In the winter of 2022-2023, California received 150% of the average rainfall through the first quarter as well as 235% of the average snowpack according to the California Water Watch program. Continued agricultural withdraws in times of drought, which are becoming both more common and intense due to climate change, will exacerbate the issues. While drought and periods of heavy precipitation have obvious consequences for water quantity, the impact of these climatic influences have been comparatively less-explored in terms of water quality and warrant further research.

California's Groundwater Ambient Management and Assessment (GAMA) Program was created in 2000 by the state's Water Resources Control Board and then expanded through the 2001 Water Quality Monitoring Act to compile historic water quality data and increase both the scale and frequency of water quality monitoring in California. GAMA is a publicly available database containing data from the United States Geologic Survey (USGS), Department of Water Resources

(DWR), Water Board, and many local groundwater projects. The goal of GAMA is to centralize groundwater quality data in a single database for the state of California so that people have access to the quality of their water source (Faunt et al., 2016; Pavley and Dickinson, 2014). In an effort to increase groundwater quality monitoring and conservation, California's state legislature passed the 2014 Sustainable Groundwater Management Act (SiGMA) (Pavley and Dickinson, 2014). The act requires local agencies in groundwater basins of high and medium priority to assemble groundwater sustainability agencies with the directive of implementing groundwater sustainability plans to mitigate excessive groundwater pumping by 2034 (Chappelle et al., 2020; Pavley and Dickinson, 2014).

2.2a Nitrate

In support of agricultural production, nitrate (NO_3^-) fertilizers and manures are heavily applied to croplands in the region (Burow et al., 2013). Following rainfall events, excess NO_3^- from fertilizer infiltrates into the subsurface along with recharge water and enters shallow groundwater (Nolan and Weber, 2015). With the infiltration of the agricultural NO_3^-, many areas throughout the valley have levels of NO_3^- in groundwater that exceed the MCL for drinking water of 10 mg/L NO_3-N set by the U.S. Environmental Protection Agency (EPA). Above this threshold, chronic exposure in infants can lead to respiratory issues including shortness of breath and blue-baby syndrome (e.g., Walton, 1951). In addition to posing its own water quality threat, elevated levels of NO_3^- may also trigger the mobilization of other contaminants contained in aquifer rocks and minerals via oxidation. For example, when NO_3^- is present in groundwater it can act as an electron acceptor and oxidize reduced uranium (U(IV)) in the mineral uraninite to its oxidized U(VI) state, which is soluble in groundwater as the uranyl ion (UO_2^{2+}).

2.2b Arsenic

Arsenic (As) is a geogenic inorganic contaminant that exists naturally in rocks, soils, and sediments. In the U.S., soils have an average As concentration of 5.2 mg/kg, where it exists mainly as the oxyanion arsenate (AsO_4^{3-}) or arsenite (AsO_3^{3-}) (Reimann et al., 2009). In drinking water, As can cause skin damage, circulatory system damage, diabetes, and an increased risk of cancer with chronic exposure to concentrations exceeding the EPA MCL of 10 µg/L (Yoshida et al., 2004). Global assessments estimate that up to 220 million people are at risk of drinking water sources exceeding the MCL, with the vast majority of those people living in Asia (Podgorski and Berg, 2020). Furthermore, chronic toxicity studies have suggested that concentrations as low as 5 µg/L can cause learning impairment in children (Wasserman et al., 2014).

Arsenic can be dissolved from aquifer minerals into groundwater via multiple mechanisms. Commonly, As exists in aquifer sediments via sorption to iron (Fe(III)) hydroxide surfaces due to strong electrostatic affinity (Pierce and Moore, 1982). Generally, below pH~8.5, Fe(III) hydroxides generate some positive surface charge which can sorb negatively charged ions (like AsO_4^{3-} and AsO_3^{3-}) out of solution. Under oxic conditions, Fe(III) hydroxides are stable, and ion removal from groundwater via sorption is a stable mechanism. However, if redox conditions become anoxic, Fe(III) in the mineral structure of hydroxides can be reduced to Fe(II), which is highly soluble as the Fe^{2+} ion. This change will cause the mineral, and any As sorbed to its surface, to dissolve into groundwater. Such changes can be facilitated by the microbial degradation of organic carbon. Given this and the pH of groundwater all Mn and Fe levels are assumed hereafter to be Mn^{2+} and Fe^{2+} respectively.

Similar to Fe(III) hydroxides, Mn(IV) oxides can also generate positive surface charge at pH near and below the point of zero net charge (7-8.5) and adsorb anions from solution (McKenzie,

1981; Stahl and James, 1991). Also like Fe(III) hydroxides, Mn(IV) in oxides can be reduced to soluble Mn^{2+} causing the release of adsorbed As into solution. While Fe(III) hydroxides are more present in higher concentrations in aquifer sediments, Mn(IV) oxides are thermodynamically preferred by microorganisms, and therefore reductive dissolution of Mn(IV) can release As into groundwater prior to the onset of Fe(III)-reducing conditions. As such, anoxic groundwater can often release As either via Mn- and/or Fe-reduction.

2.2c Uranium

Uranium (U) is a geogenic inorganic contaminant in groundwater. Acute contamination is common from U mining sites (Abdelouas, 2006). Chronic exposure to U concentrations exceeding the MCL (30 µg/L) can lead to kidney toxicity and an increased risk of cancer (Voegtlin and Hodge, 1953). U contamination is a global threat to groundwater with contamination found in the United States, Asia and India, among other regions (Guo et al., 2018; Jakhu et al., 2016; Thiros et al., 2014). U contamination is also a threat in the United States (U.S.); the USGS reports that measurable U contamination (< 0.003 µg/L) is present in 35% of United States drinking water wells, and many wells in the western U.S. exceed the MCL (DeSimone et al., 2014; Thiros et al., 2014).

Unlike As, which is typically mobilized under reducing conditions, U is more mobile if groundwater is oxidizing. Generally, U can be mobilized via the oxidation of U(IV) in minerals weathered from mafic and ultramafic rocks (e.g., uraninite (UO_2) to the U(VI) oxycation, uranyl (UO_2^{2+})). Typically, either O_2 (Eq. 3) or NO_3^- (Eq. 4) acts as the electron acceptor due to high energy yields. While O_2 is thermodynamically favorable, in its absence NO_3^- can also oxidize U(IV) shown in Equation 3 and 4 below:

$$UO_{2\,(s)} + 2\,H^+ + 0.5\,O_{2\,(aq)} \rightarrow UO_{2\,(aq)}^{2+} + H_2O \qquad\qquad \text{logK} = 29.25 \qquad\qquad \text{Eq. 3}$$

$$UO_{2\,(s)} + 1.2\,H^+ + 0.4\,NO_3^- \rightarrow UO_{2\,(aq)}^{2+} + 0.8\,H_2O + 0.2\,N_2 \qquad \text{logK} = 27.80 \qquad\qquad \text{Eq. 4}$$
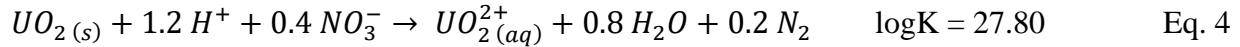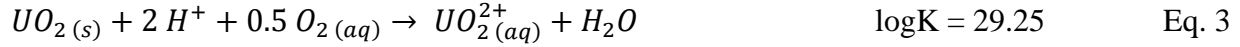
Like As, U, once mobilized as $UO_2{}^{2+}$, can be removed from groundwater via sorption to Fe hydroxides. Generally, above pH 7, hydroxides can generate some negative surface charge, to which a positively charged $UO_2{}^{2+}$ ion can be sorbed and removed from groundwater (Abdelouas, 2006; Zheng et al., 2003). However, if the hydroxides that are keeping U out of groundwater are exposed to reducing conditions, then both the charged $UO_2{}^{2+}$ ion and Fe^{2+} will be mobilized into groundwater.

U solubility can be enhanced in the presence of carbonate ($CO_3{}^{2-}$) via the formation of several aqueous uranium-carbonate complexes as shown in Equations 3-7 (Langmuir, 1997). Furthermore, recent research has shown that ternary aqueous calcium uranyl carbonate complexes further enhance U solubility as shown in Equations 8-9 (Dong and Brooks, 2006).

$$UO_2{}^{2+} + CO_3{}^{2-} \rightarrow UO_2CO_3{}^{\circ}{}_{(aq)} \qquad\qquad \text{logK} = 9.67 \qquad\qquad \text{Eq. 5}$$

$$UO_2{}^{2+} + 2CO_3{}^{2-} \rightarrow UO_2(CO_3)_2{}^{2-}{}_{(aq)} \qquad\qquad \text{logK} = 16.99 \qquad\qquad \text{Eq. 6}$$

$$UO_2{}^{2+} + 3CO_3{}^{2-} \rightarrow UO_2(CO_3)_3{}^{4-}{}_{(aq)} \qquad\qquad \text{logK} = 21.64 \qquad\qquad \text{Eq. 7}$$

$$UO_2{}^{2+} + Ca^{2+} + 3CO_3{}^{2-} \rightarrow CaUO_2(CO_3)_3{}^{2-}{}_{(aq)} \qquad\qquad \text{logK} = 3.63 \qquad\qquad \text{Eq. 8}$$

$$UO_2{}^{2+} + 2Ca^{2+} + 3CO_3{}^{2-} \rightarrow Ca_2UO_2(CO_3)_3{}^{\circ}{}_{(aq)} \qquad\qquad \text{logK} = 6.29 \qquad\qquad \text{Eq. 9}$$
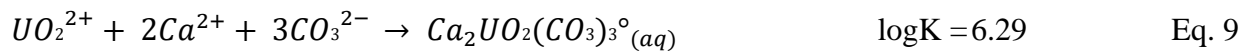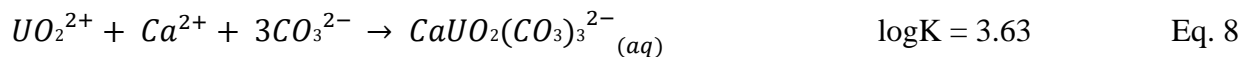
The formation of these complexes creates either neutrally or negatively charged U species, which inhibits U sorption and stabilizes U in groundwater.

The processes that promote As and U mobility in groundwater are geochemically complex and can often vary over space and time. Given the reliance of central California on groundwater quality for drinking water, irrigation, as well as other industries, I seek to:

1. identify the spatial extent of groundwater contamination with regards to As and U in three dimensions (i.e. shallow vs. deep groundwater);

2. use geochemical and statistical models to infer the geochemical mechanisms that mobilize As and U into groundwater;

3. evaluate the water quality vulnerability in the shallow and deep aquifers under different climactic conditions as a proxy for future environmental change.

3. Methods

3.1 Groundwater data acquisition and filtering

I acquired groundwater well chemistry data for 2005-2018 from the GAMA Program database. I focused on this time period because it represented four oscillations between drought and non-drought periods (Fig. 2). Parameters extracted from the GAMA database included well latitude, longitude, depth (when reported), alkalinity, As, Ca^{2+}, dissolved oxygen (D.O.), Fe^{2+}, Mg^{2+}, Mn^{2+}, NO_3–N, pH, specific conductivity (S.C.), SO_4^{2-}, and U. Alkalinity was assumed to be a proxy measurement of HCO_3^- and/or CO_3^{2-}. Other proton acceptors were assumed to be comparatively negligible. I attempted to remove wells that were monitoring anthropogenic point sources of pollution (i.e., spills) or wells that were installed in the vadose zone so that I was considering only phreatic groundwater representative of broader aquifer processes. Wells that were monitoring the vadose zone or above the thresholds listed in Table 1 were assumed above any reasonable concentrations for typical geogenic processes, and thus were removed.

Parameter	Geogenic Threshold
Alkalinity	2000 (mg/L)
As	500 (μg/L)
Ca^{2+}	2000 (mg/L)
Cl^-	10,000 (mg/L)
D.O.	14 (mg/L)
Fe^{2+}	100 (mg/L)
Mg^{2+}	10 (g/L)
Mn^{2+}	100 (mg/L)
Na^+	10,000 (mg/L)
NO_3-N	500 (mg/L)
pH	14 (pH units)
S.C.	100,000 (μΩ/cm)
SO_4^{2-}	10 (g/L)
T.D.S.	30,000 (mg/L)
U	400 (pCi/L)

3.2 Statistical Analysis

I performed a principal component analysis (PCA) for wells that contained a reported value

for each of the following parameters from a single sampling event: alkalinity, As, Ca^{2+}, Cl^-, D.O.,

Fe^{2+}, Mg^{2+}, Mn^{2+}, Na^+, NO_3–N, pH, S.C., SO_4^{2-}, T.D.S, and U (n = 105). Parameters As, Ca^{2+}, Cl^-

, Fe^{2+}, Mg^{2+}, Mn^{2+}, Na^+, NO_3–N, SO_4^{2-}, T.D.S, and U were log-normally distributed and therefore

the molar concentrations of these parameters were log-transformed. D.O., S.C., and alkalinity were normally distributed and were used as reported. pH was normally distributed and was translated to negative pH to reflect $\log[H^+]$. Each normally distributed dataset was then scaled from zero to one with Eq. 10 to reduce the impact of concentration magnitude (e.g., U generally ranging from 0 to 10s of μg/L while alkalinity was often > 100s of mg/L) where X denotes a specific chemical. Normalized, scaled data were then used for PCA in R Studio (4.1.0).

$$\frac{[Value\ (X) - Min(X)]}{[Max\ (X) - Min\ (X)]}$$

Eq. 10

3.3 Spatial Analysis

In my spatial analysis, I used data from any well sampled between 2005 and 2018 with a reported value for any of the aforementioned parameters. Because on a particular sample date GAMA may report only one chemical or several chemicals, the specific wells used for the spatial analysis of each chemical constituent differed from each other. For wells with reported values for a parameter from multiple sampling events, I used the maximum value, with the exception of D.O., because the collection method for D.O. often introduces atmospheric oxygen producing values that are artificially inflated (White et al., 1990). Thus, I used the lowest recorded D.O. value when multiple values were reported.

Well data were split into "shallow" and "deep" wells following the method of Burow et al. (2013). First, wells with reported depths were identified and separated from wells lacking a reported depth. Using wells with known depths, municipal and public supply wells were categorized as deep wells due to their high withdrawal needs and long screens, and monitoring and domestic wells were categorized as shallow wells. For the three chemical datasets with the most complete depth information (alkalinity, NO_3-N, and SO_4^{2-}), I found the third quartile for well depth

from the shallow wells (average of the three datasets was 27 m below land surface) and the first

quartile for well depth from the deep wells (average of the three datasets was 92 m below land

surface). The midpoint of third quartile for shallow wells and first quartile for deep wells was

calculated for alkalinity, NO_3-N, and SO_4^{2-} wells. The average of the midpoint of the three datasets

(60 m) was used as the threshold to separate "shallow" from "deep" groundwater. When well depth

was not reported, I used the reported well type to categorize a well as shallow or deep. I

characterized monitoring and domestic wells as shallow wells and municipal and public supply

wells as deep wells.

To assess the impact of climate variability on water quality, I separated the 2005-2018 data

into four time-range subsets, each representing a drought or non-drought period. I tested drought

impacts in two ways: the first approach compared drought vs non-drought conditions and the

second compared drying conditions (i.e., trending toward drought) vs wetting conditions (i.e.,

trending toward non-drought). To determine the timing of those cycles, I consulted the Palmer

Drought Severity Index (PDSI) for the SJV shown
in Figure 2 (Faunt et al., 2016; Levy et al., 2021).
Droughts were quantified as times when the PDSI
was less than -1 and non-drought was when the
index was greater than -1 (rounding to the nearest
year). Wetting and drying periods were determined
from the inflection points of the PDSI trendline
(i.e., negative slopes were categorized as drying
periods; positive slopes were categorized as
wetting periods). The resulting date ranges (Table
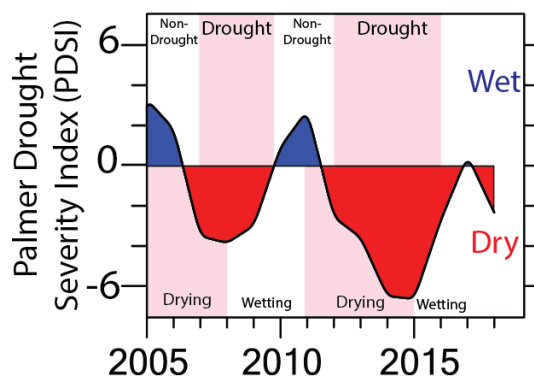
Figure 2. Palmer Drought Severity Index for the San Joaquin Valley with red bands above the axis that denote droughts and below the axis that denote drying. Modified from Levy et al. 2021.

2) were used to bin well concentration data for drought/non-drought cycles and wetting/drying cycles.

Table 2. Table showing the time ranges that were delineated based on data from Levy. et al. 2021 and Faunt et al. 2016.

Cycle	Time Ranges			
Drought/Non-Drought	2005-2007	2007-2010	2010-2012	2012-2017
	Non-Drought	Drought	Non-Drought	Drought
Wetting/Drying	2005-2008	2008-2011	2011-2015	2015-2018
	Drying	Wetting	Drying	Wetting

After separating well data by depth and time, I made shapefile feature classes in ArcGIS Pro (3.0.1) for each chemical parameter at both shallow and deep depths for the four drought/non-drought year ranges and the four wetting/drying year ranges, totaling sixteen shapefiles per chemical parameter. The shapefiles were then clipped to match the extent of the CV to exclude any non-CV data. The shapefiles were then projected from WGS 1984 global coordinate system into UTM-Zone 11N projected coordinate system which is the local projected coordinates for California. I performed Empirical Bayesian Kriging (EBK) on each feature class to create a smoothed surface of concentration according to the parameters in Table 3. The output of the EBK interpolation is a rasterized map from the geostatistical interpolation.

Table 3. EBK parameters used to krig the CV interpolations

Empirical Bayesian Kriging (EBK) Parameters	\<Value\>
Raster Cell Size	1000 x 1000m
Data Transformation Type	Empirical
Max. Number of Points in Each Local Model	200
Local Model Area Overlap Factor	2.5
Number of Simulated Semivariograms	7500
Search Neighborhood Type	Smooth Circular
Search Neighborhood Radius	3500
Smoothing Factor	0.2
Semivariogram Model Type	K_BESSEL_DETRENDED

EBK is a machine-learning approach to two-dimensional interpolation that results in less error and more accurate interpolation than ordinary kriging or inverse distance weighting models. EBK surfaces had lower standard error and a standardized root mean squared closer to 1. Furthermore, the input values can be standardized across all of the chemical parameters studied to eliminate human error and bias into the interpolation scheme. This approach produces more accurate results and involves less human interaction but requires substantially more computation time and power and does not account for anisotropy, which is present in the CV (Krivoruchko and Gribov, 2019).

3.4 Density Plots

I extracted As and U values from the rasters with latitude, longitude, and concentration linked. I wrote a Python script to separate the data at 4,250,000 (UTM Zone 11), a proxy for the separation of the SJV and SV, and then plotted the data using kernel density estimation (KDE) (Rosenblatt, 1956). I distinguished time periods, depths, and the separation of the SJV and SV.

3.5 Uranium Correlation Raster Analysis in the Kings Groundwater Basin

The Kings Groundwater Basin (KGWB; see Figure 1 for location in the CV) was the only groundwater basin with high levels (>30 µg/L) of U. To elucidate U mobilization mechanisms, I performed a correlation analysis between U and various parameters that might participate in U mobilization reactions (Eq. 4-5), either as a reactant or a product (NO_3^-, D.O., Ca^{2+}, alkalinity, pH, Fe^{2+} and U). To do this, I used raster maps of kriged concentrations in the KGWB in 2005-2017, though I limited modeling to the drought/non-drought time periods (Table 2). For interpolation, I used ordinary kriging in the geostatistical wizard of ArcGIS according to the parameters in Table 4. Parameters were manipulated by hand to result in the smallest error as measured by standardized root mean square and average standard error, just as the EBK maps were chosen. I used a similar data cleaning and depth splitting approach described previously and found the separation between shallow and deep groundwater to be 74.3 m below land surface in the KGWB.

Resulting feature classes were then rasterized at a resolution of (1x1 km). Log-normally distributed layers (denoted by a log transformation in Table 4) were log-transformed to generate a normal distribution during rasterization. Layers that were normally distributed were used with raw concentrations. The values for each raster output were then scaled from 0 to 1 using Eq. 11.

$$X_\alpha^{Scaled} = \frac{[X_\alpha - X_{min}]}{[X_{max} - X_{min}]}$$

Eq. 11

Table 4. The geostatistal parameterization used for ordinary kriging for each constituent within the shallow and deep aquifers of the KGWB.

Chemical	Depth	Transformation	Trendline Removal	Lag (m)	Number of lags	Anisotropy (°E of N)	Major range (m)	Minor range (m)	Nugget/sill
Alkalinity	shallow	log	first	6574	12	60	52,594	13.681	T/T
	deep	log	first	3479	12	65	41,746	17,334	
Ca^{2+}	shallow	log	first	1500	12	139	10,642	3626	T/T
	deep	log	first	4500	12	137	54,000	30,030	
DO	shallow	none	first	5264	12	138	60,516	30,904	T/T
	deep	none	first	2764	12	141	33,167	18,638	
Fe^{2+}	shallow	log	first	4929	12	83	59,149	19,772	T/T
	deep	log	first	7000	12	131	84,000	28,786	
NO_3-N	shallow	log	first	2120	12	81	8735	2918	T/T
	deep	log	first	4150	12	138	49,800	29,447	
pH	shallow	none	first	3243	12	31	15,463	5176	T/T
	deep	none	first	3859	12	176	33,812	27,909	
U	shallow	log	constant	8475	12	N/A	63,721	N/A	T/T
	deep	log	first	7000	12	132	84,000	28,291	

To evaluate the spatial correlation of U (dependent variable) with other potential explanatory variables (e.g. NO_3-N, D.O., H^+, Fe^{2+}, Ca^{2+}, alkalinity), each scaled chemical raster map was masked to the spatial extent of where concentrations of U were ¼ of the MCL (7.5 µg/L) to only evaluate regions where U was present at considerable concentrations. Comparisons between two scaled layers (e.g., NO_3-N and U) were performed for each raster cell using Eq. 12,

which creates an output value of zero (no correlation) to one (high correlation) between the scaled

parameters X and Y for each raster cell where $corr_{i,j}$ is the correlation in cell i,j.

$$corr_{i,j} = 1 - \left| X_{i,j}^{scaled} - Y_{i,j}^{scaled} \right| \qquad \text{Eq. 12}$$

3.6 Carbonate Complexation Modeling in the Kings Groundwater Basin

I developed a workflow to model the formation of aqueous complexes of U(VI) by CO_3^{2-}

and Ca^{2+} with CO_3^{2-} (Eqs. 5-9) using the rasterized concentration maps for alkalinity, Ca^{2+}, pH,

and U. For each concentration raster, I extracted the concentration from each cell for each

aforementioned parameter from ArcGIS Pro using the R-ArcGIS bridge. Those values were then

converted into tabular data preserving the UTM coordinates and concentration of the chemical

parameter for each cell in the raster. After compiling the chemical parameters, I imported the data

into The Geochemist's Workbench (Community Edition 16.0) Spec8 module to geochemically

model the equilibrium concentrations UO_2^{2+}, $UO_2CO_3^0$, $UO_2(CO_3)_2^{2-}$, $UO_2(CO_3)_3^{4-}$,

$CaUO_2(CO_3)_3^{2-}$, $Ca_2UO_2(CO_3)_3^0$ (Eqs. 5-9). I used the Lawrence Livermore National Laboratory

thermodynamic database appended with additional reactions (Eqs. 8-9) and equilibrium constants

determined by Dong and Brooks (2006). I then wrote a Python (3.11) script to extract the

concentrations of the products of Equations 5-9 and then compiled them into a single table listing

the concentration and UTM coordinates. I then converted the tables into rasters in R-Studio and

imported them into ArcGIS Pro to be spatially referenced.

4. Results

4.1 Statistical Analysis
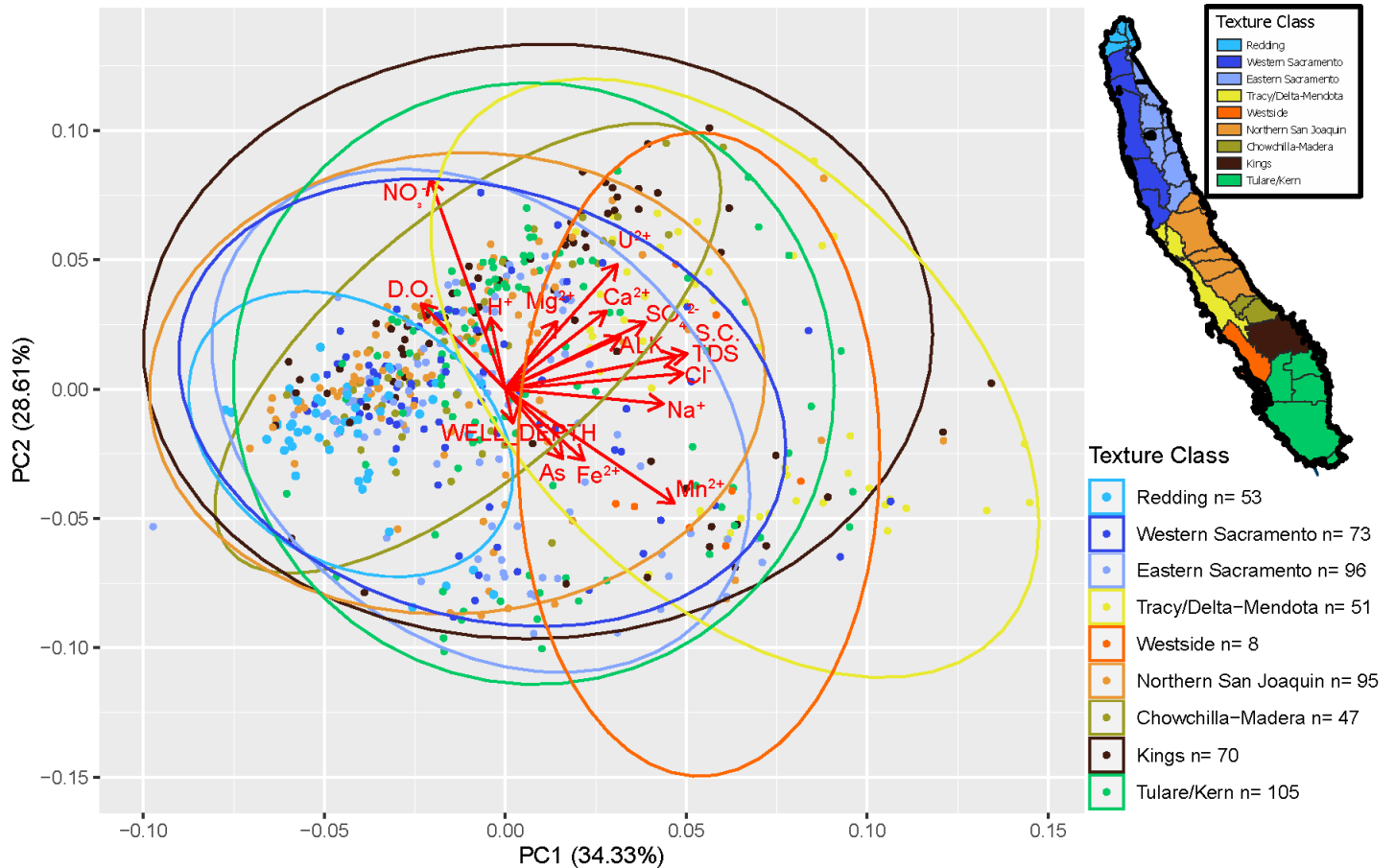
Figure 3. *Principal Component Analysis (PCA) from well data with coloration and grouping for textural class by geography, with spatial reference to the CV in the top right. Red arrows indicate chemical parameters relation to PC1 and PC2.*

Using the data extracted from GAMA for statistical analysis, I constructed a data set of the complete suite of chemical parameters for a specific well sampled on a specific date. Using these data, I performed a PCA (Figure 3). In the PCA, vectors (red arrows) represent how much influence a parameter has on a principal component (PC): where PC1 falls on the x-axis, and PC2 falls along the y-axis. A vector more parallel to a PC axis is more strongly related to that PC, and a longer vector exerts more control in the vector's direction. The points, colorized by textural class of the

well location in Figure 1, represent the coordinates of a well sample's chemistry in the PC dimensions. PC1 describes 34.33% of the variability in the overall dataset. The most closely related (most parallel) vectors to PC1 are Na^+, Cl^-, T.D.S., and S.C. along with lesser control by alkalinity, As, Ca^{2+}, Fe^{2+}, Mg^{2+}, Mn^{2+}, pH, S.C., SO_4^{2-}, and U. Species exerting most control on PC1 are charged ionic species and major ions in solution, and thus, contribute the majority of the solution's ionic strength, for which T.D.S. and S.C. (two of the most related species) are proxies. In contrast there is a lack of vectors in the negative PC1 dimension. While D.O., and to a lesser extent NO_3^-, occur in the negative PC1 dimension, they are generally orthogonal to the PC1 axis and thus exert little control on PC1.

PC2 has much more diversity than PC1 with many vectors in both directions. In the positive PC2 dimension, chemical species listed in order of influence are NO_3^-, D.O., H^+, U, Mg^{2+}, Ca^{2+}, and others that have less influence (as defined by length and angle relative to the axis). In the negative PC2 dimension, parameters listed in order of influence are Mn^{2+}, Fe^{2+}, As, and well depth. Furthermore, there is a ~180° relationship between the NO_3^-/ D.O./ H^+ cluster and the Mn^{2+}/Fe^{2+}/As/well depth cluster.

Most textural class regions show little bias to either side of PC1. However, groundwater samples from Redding are completely negative, and Westside groundwater samples are completely positive. Tracy/Delta-Mendota also seems to have some bias towards the positive PC1 space. All three are in the western half of the valley which is largely weathered from the Coastal Range. In the PC2 dimension, few textural classes favor either the positive or negative dimension by spanning both. Because well depth appears related to PC2, and because each region had samples from shallow wells and deep wells, a region spanning the range of PC2 values is unsurprising.

4.2 Spatial Analysis

4.2.1 Arsenic

4.2.1a Drought/Non-Drought Cycle

Kriged As concentrations over time are shown Figure 4 (included on the next page) for both the shallow (A-D) and deep (E-H) aquifers. Time ranges include a non-drought period from 2005-2007 (Figure 4A and 4E), a drought period from 2007-2010 (Figure 4B and 4F), a non-drought period from 2010-2011 (Figure 4C and 4G), and a drought period from 2012-2015 (Figure 4D and 4H). For the first time period, 2005-2007 non-drought, As concentrations in the CV are above the MCL (10 µg/L) in 32% of the shallow aquifer and 25% in the deep aquifer. In 2007-2010 drought concentrations increased in both aquifers to 58% in the shallow aquifer and 28% in the deep aquifer. In the 2010-2012 non-drought period contamination decreases to 37% in the shallow aquifer and 18% in the deep aquifer. In the 2012-2017 drought, As concentrations continue to improve with only 25% of shallow aquifer and 15% of deep aquifer interpolation values exceeding the MCL.

In the shallow aquifer, the spatial occurrence As > 10 µg/L is variable, with the region of contamination shifting over time (Figure 4). In the SJV, contamination seems to first expand from 2005-2007 (Figure 4A) into 2007-2010 (Figure 4B) and then improve in the latter two time periods with the spatial extent of the valley which exceeds 10 µg/L decreasing (Figure 4C and D). In the SV, the spatial extent of As exceeding 10 µg/L worsen with 2012-2017 being the worst. The expanse of the spatial extent of As contamination in the north is particularly present in the transition from 2005 to 2007 and then again from 2010 to 2012, which corresponds to the transition from non-drought to drought. The apparent northwards migration of As contamination is also seen
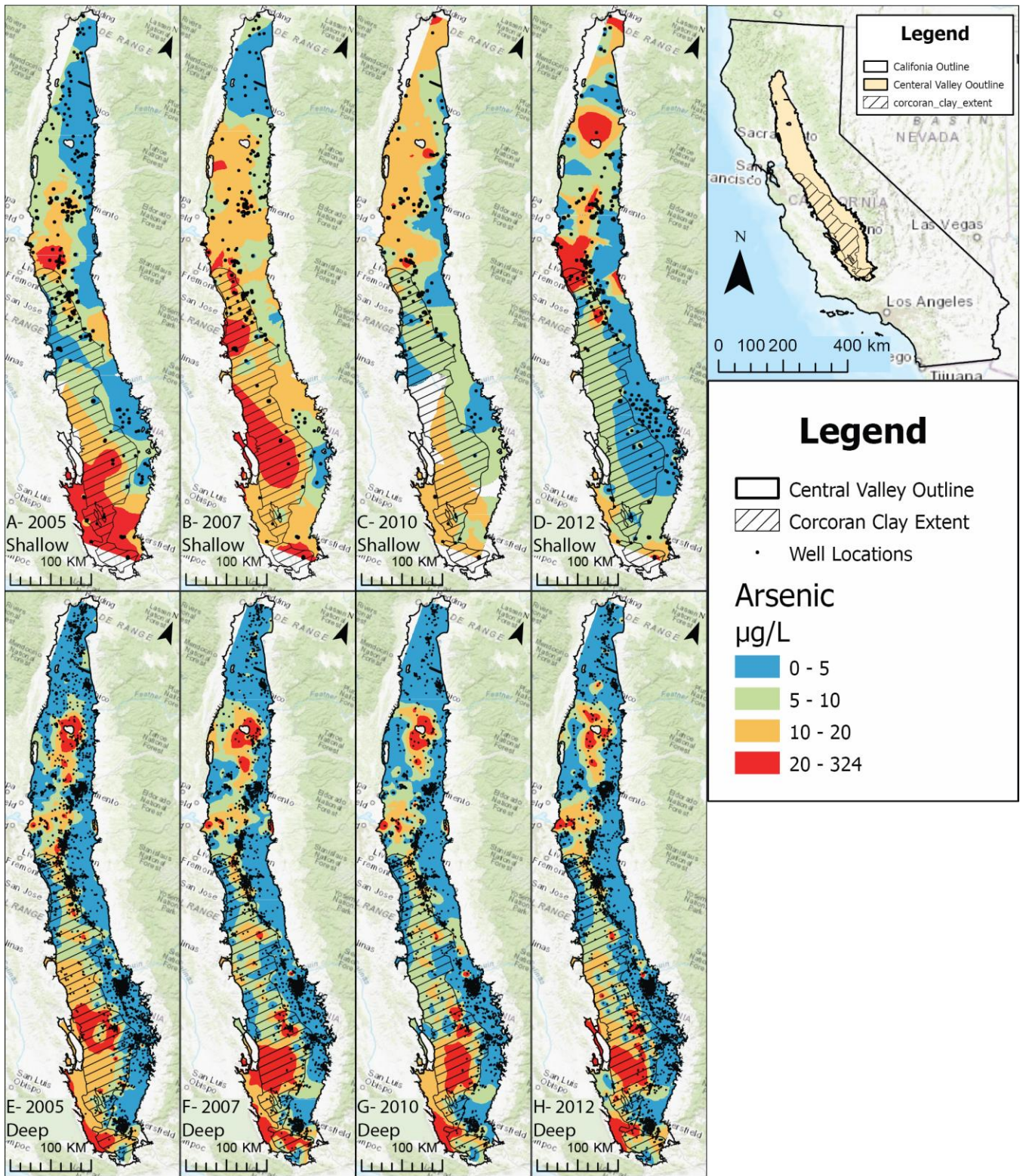
Figure 4. *Spatial analysis showing As concentrations in the CV by coloration contours. Locations where well data was known are indicated by black dots, and the extent of the Corcoran Clay is cross hatched.*

in Figure 5 in the density plots. The dotted lines represent all values north of 4,250,000 m northing
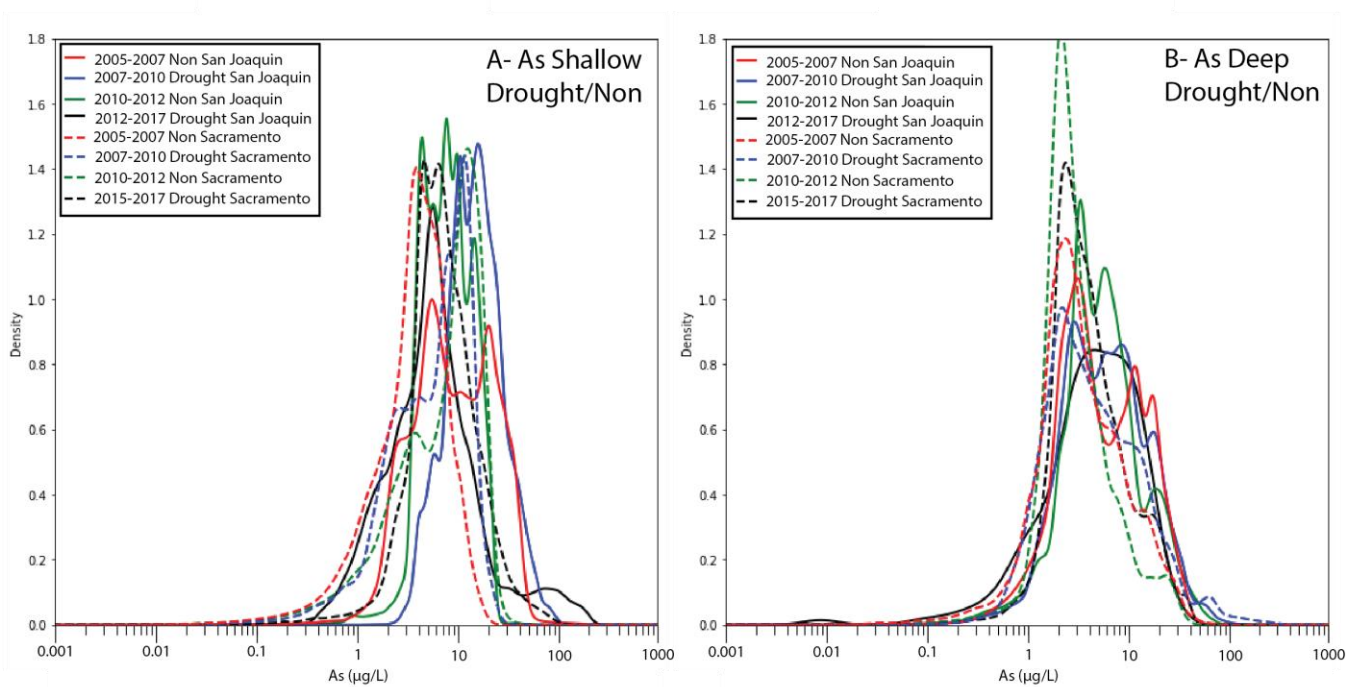
Figure 5. *Density functions of the raster cells from Figure 6 in the shallow (A) and deep (B) aquifers throughout time for the north (Sacramento(dotted) and South (San Joaquin(solid) basins. The time breaks are defined by the Drought/Non-Drought cycle in Figure 3.*

(UTM Zone 11), which is an approximation of the southern boundary of the SV, and the solid lines represent values south of the boundary, which is an approximation of the northern extent of the SJV. We see in shallow groundwater data from the SJV that the worst year for As contamination is 2007 (solid blue), indicated by the highest density of high values (taller peak on the right side). In the north, we see the opposite trend where the highest concentrations (20-30 µg/L) occur at a greater frequency as time progresses. From this, it appears that the shallow SJV groundwater is variable, and contamination is changing throughout time, whereas As in the shallow SV appears to worsen in times of drought. Correlations are minimal between As (Figure 4), Fe^{2+} (Figure 6) and Mn^{2+} (Figure 7) in shallow groundwater. One possible explanation is that Fe-reduction has occurred enough to release Fe^{2+} to concentrations great enough to pose a drinking water concern (above the MCL = 300 µg/L), while not enough Fe-reduction has occurred to release As into
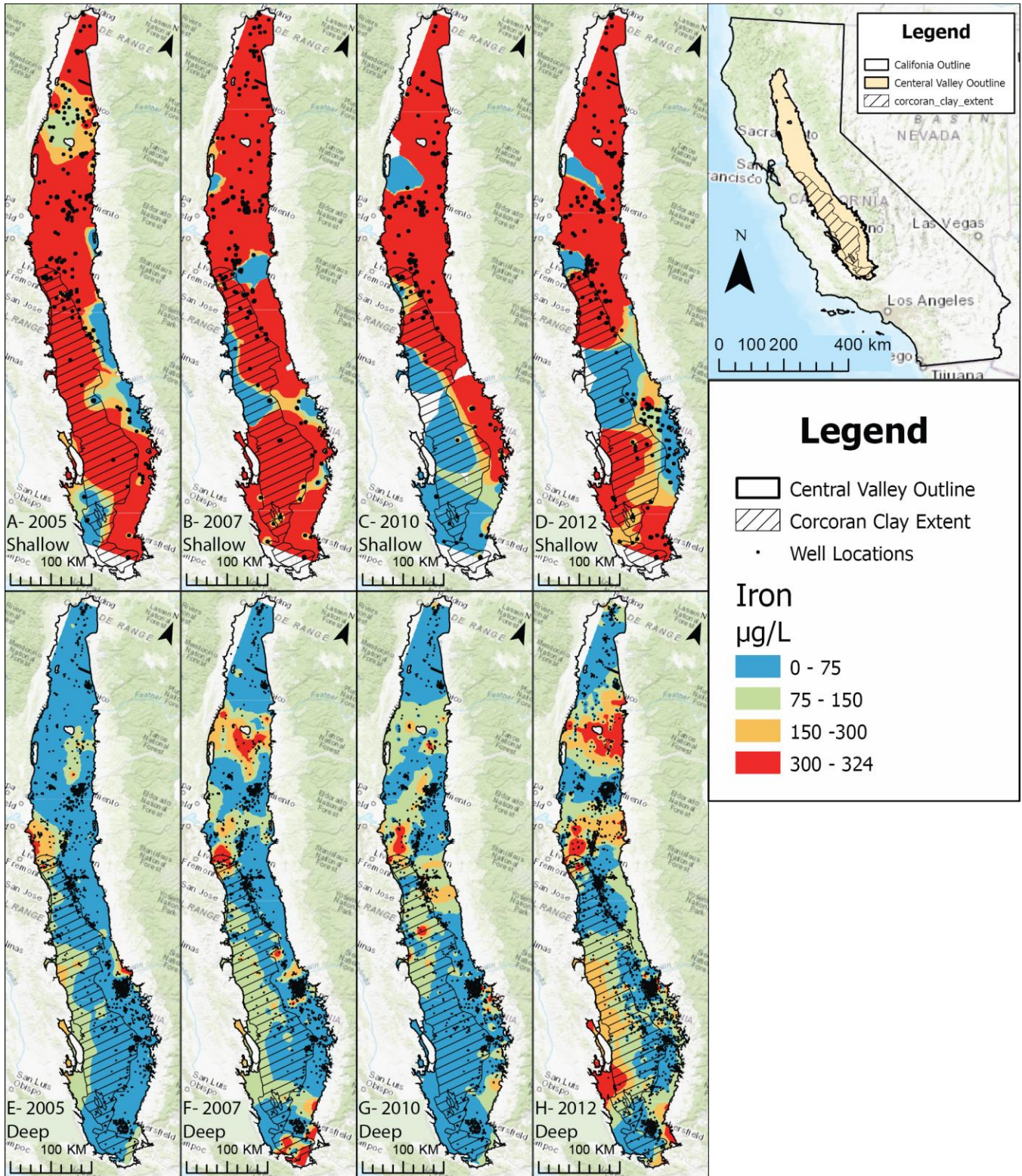
Figure 6. *Spatial analysis showing Fe concentrations in the CV by coloration contours. Locations where well data was known are indicated by black dots, and the extent of the Corcoran Clay is cross hatched.*
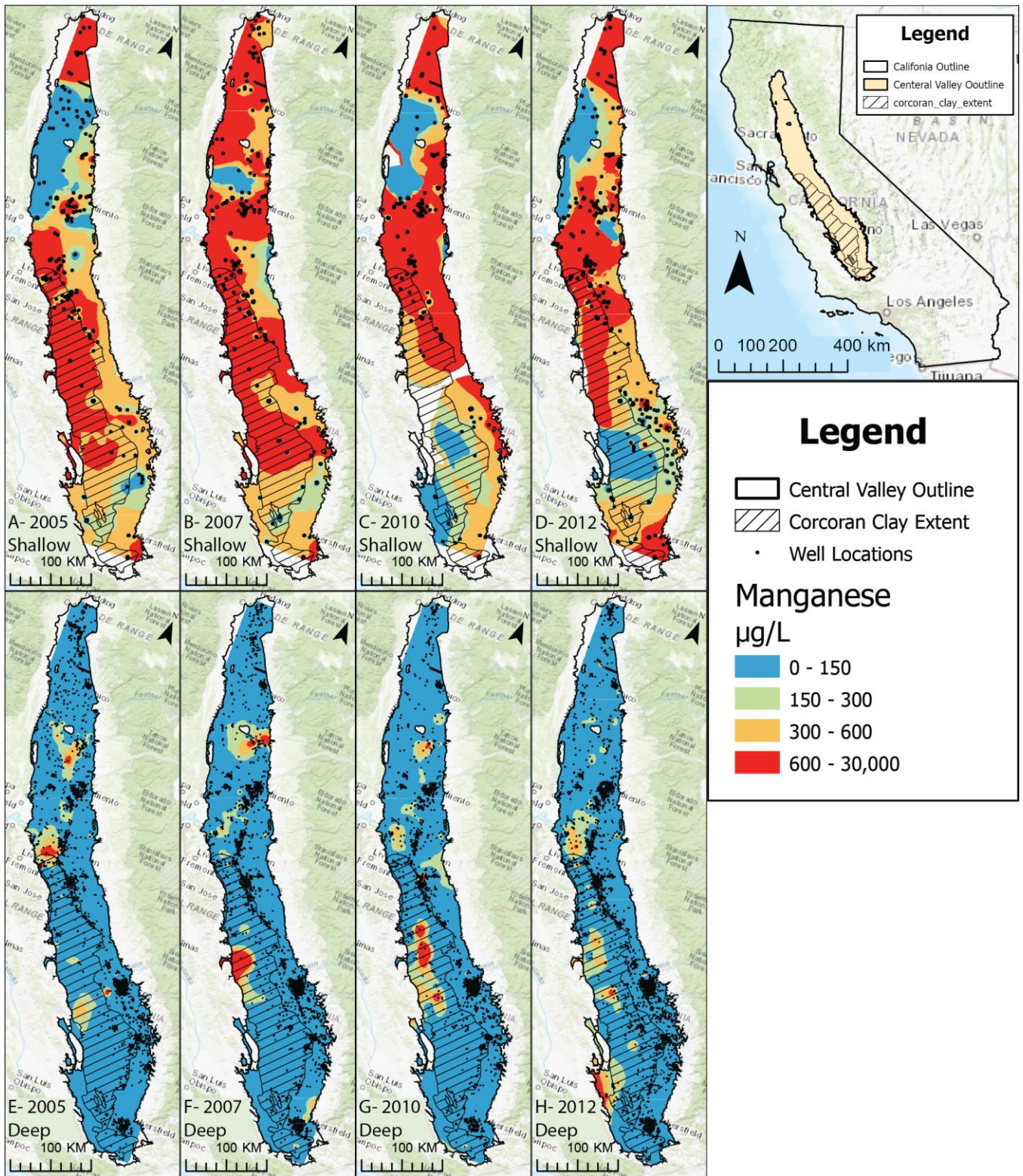
Figure 7. Spatial analysis showing Mn concentrations in the CV by coloration contours. Locations where well data was known are indicated by black dots, and the extent of the Corcoran Clay is cross hatched.

groundwater. A second possible explanation is that the variations that we see with As contamination in the shallow aquifer are present with Fe^{2+} but cannot be observed because of the coloration I chose to make the deep Fe^{2+} map readable. However, it is important to note that modeling both Fe^{2+} and Mn^{2+} proved exceptionally difficult with high error values and inconsistent results. Additionally, note that while there are locations with elevated Fe^{2+} but not As, the reverse is not the case.

In the deep aquifer, As concentrations are much more consistent over space and time compared to the shallow aquifer (Figure 4E-H; Figure 4A-D). Over time there is limited change in the spatial extent of As contamination in deep aquifer interpolations (Figure 4E-H). The SJV contamination spatially mimics the extent of the Corcoran Clay unit (indicated by the crosshatched pattern in Figure 4). Deep aquifer Fe^{2+} values are low with the exception of data from 2012-2017, which displays some contamination under the Corcoran Clay. In the deep SV aquifer, however, Fe^{2+} trends are similar to As in space and time, with high levels in the central SV. Fe^{2+} concentrations in deep groundwater seem to be more sensitive to the drought cycle, displaying a similar trend to the shallow As data. Contamination worsens, both in spatial extent and magnitude in the transition from the 2005-2007 non-drought (Figure 6E) to the 2007-2010 drought (Figure 6F), then improves into the 2010-2012 non-drought (Figure 6G) before worsening again in the 2012-2017 drought (Figure 6H). Elevated concentrations of Mn^{2+} are less common and spatially more sporadic than Fe^{2+} in the deep aquifer, although inconsistent regions of elevated Mn^{2+} occurs in regions with elevated Fe^{2+} and As at the northern edge of the Corcoran Clay, near the center of the Corcoran Clay to the west, and in the northern SV. The correlation between As and Mn^{2+} in the deep is poor, although when Mn^{2+} is elevated in groundwater, As also tends to be elevated, though the reverse is not necessarily true.

4.2.1b Wetting/Drying Cycle

To evaluate whether groundwater As concentrations displayed greater sensitivity to wetting/drying cycles compared to drought/non-drought cycles, I replicated the analysis described in Section 4.2.1a with the wetting/drying time breaks defined in Table 2. Density plots in Figure 8
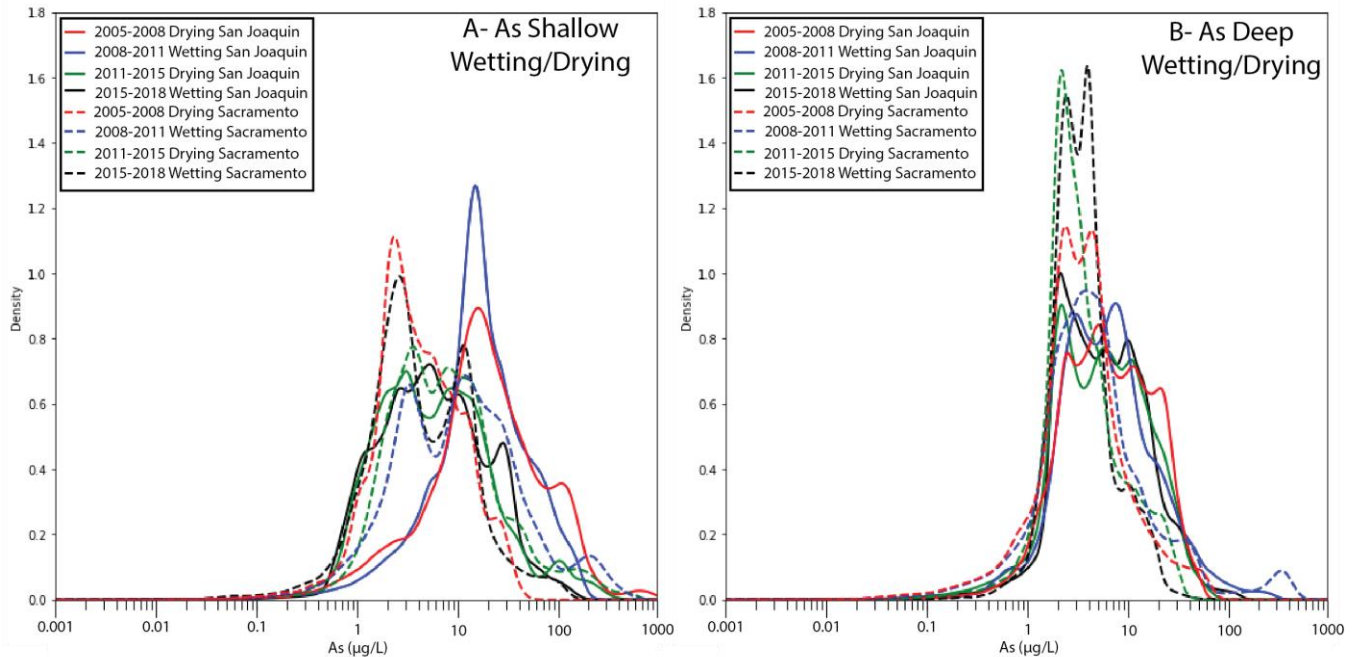
Figure 8. Density functions of the raster cells from Figure 6 in the shallow (A) and deep (B) aquifers throughout time for the north (Sacramento(dotted) and South (San Jaquin(solid) basins. The time periods are defined by the Wetting/Drying cycle in Figure 3.

show broader peaks than in Figure 5 but also higher As concentrations closer to 1000 µg/L. In the shallow aquifer, Figure 8A shows a similar trend to the drought/non-drought data with a relative increase in As contamination in the southern SJV over time (solid lines) as compared to the SV (dashed lines). In the SJV, the 2005-2008 drying and 2008-2011 wetting period are similar, whereas the 2011-2015 drying and 2015-2018 wetting periods are skewed to lower concentrations. In the SV (dotted lines), the levels of contamination listed in descending order begins with the 2008-2011 wetting period, then the 2011-2015 drying period, the 2015-2018 wetting period, and lastly the 2005-2008 drying period (Figure 8). The trends seen in Figure 8 hold true spatially as

Figure 9. Spatial analysis showing As concentrations in the CV by coloration contours in the wetting drying cycle. Locations where well data was known are indicated by black dots, and the extent of the Corcoran Clay is cross hatched.

well (Figure 9). However, it appears that As contamination increases during drying periods and then decreases with inflow of fresh water with the start of the new wetting phase. Although this trend is based on only two repetitions of the cycle, conceptually it makes sense that oxygenated water would decrease the extent of As contamination. In the SJV, As contamination spatially seems to improve in shallow groundwater, whereas in the SV, As contamination seems to worsen as time progresses, and shallow As concentrations become more similar to the deep aquifer.

In the deep aquifer, contamination is relatively consistent when compared to the shallow aquifer. The SJV displays a broader concentration distribution with higher values more common than in the SV. There is an anomalous peak around 250 µg/L As in the 2008-2011 wetting period in the SV. The stability seen in the spatial distribution of drought/non-drought deep aquifer data (Figure 4E-H) is consistent with the wetting/drying data in Figure 9E-H. Regardless of the grouping of years, high As contamination is present under the Corcoran Clay in the SJV. A hotspot of consistently elevated As occurs in the north-central SV.

4.2.3 Uranium

4.2.3.1 Uranium Valley Wide Observations

4.2.3.1a Drought/Non-Drought Cycle

Shallow modeling of U concentrations (Figure 10 A-D) was limited due to a lack of available data from GAMA, especially for the years 2007-2012. For the drought/non-drought cycle there were sufficient data to make meaningful conclusions only in the 2005-2007 and 2012-2017 periods. Contamination in the 2005-2007 non-drought period was limited to the western edge of the Kings Groundwater Basin (KGWB). While there appears to be moderate levels of U present in the more northern sections in the 2012-2015 drought period, this is likely due to a single elevated well without other data to inform the region.

In the deep aquifer (Figure 10 E-H), there are moderate levels ($> 30\mu g/L$) of U throughout the SJV generally at the edge of the Corcoran Clay extent. However, the only two areas that exceed the MCL for more than one period are a single well in the SV and in the western KGWB. The single well in the SV was anomalous relative to the surrounding well data, thus I chose to not include it in further modeling as it is difficult to make meaningful interpretations from one datum.

4.2.3.1b Wetting/Drying Cycle

The wetting/drying cycle (2008-2015) had a slightly more even distribution of data, allowing for better coverage in the shallow aquifer, yet the only high U values were in the western KGWB (Figure 11). Elevated U in the deep aquifer was generally limited to the KGWB as well, with a few wells exceeding the MCL. In the deep aquifer, U concentrations appear to increase in severity from the 2005-2008 wetting to the 2008-2011 drying and then further deteriorate into the 2011-2015 wetting period before slightly improving in the 2015-2018 drying period.
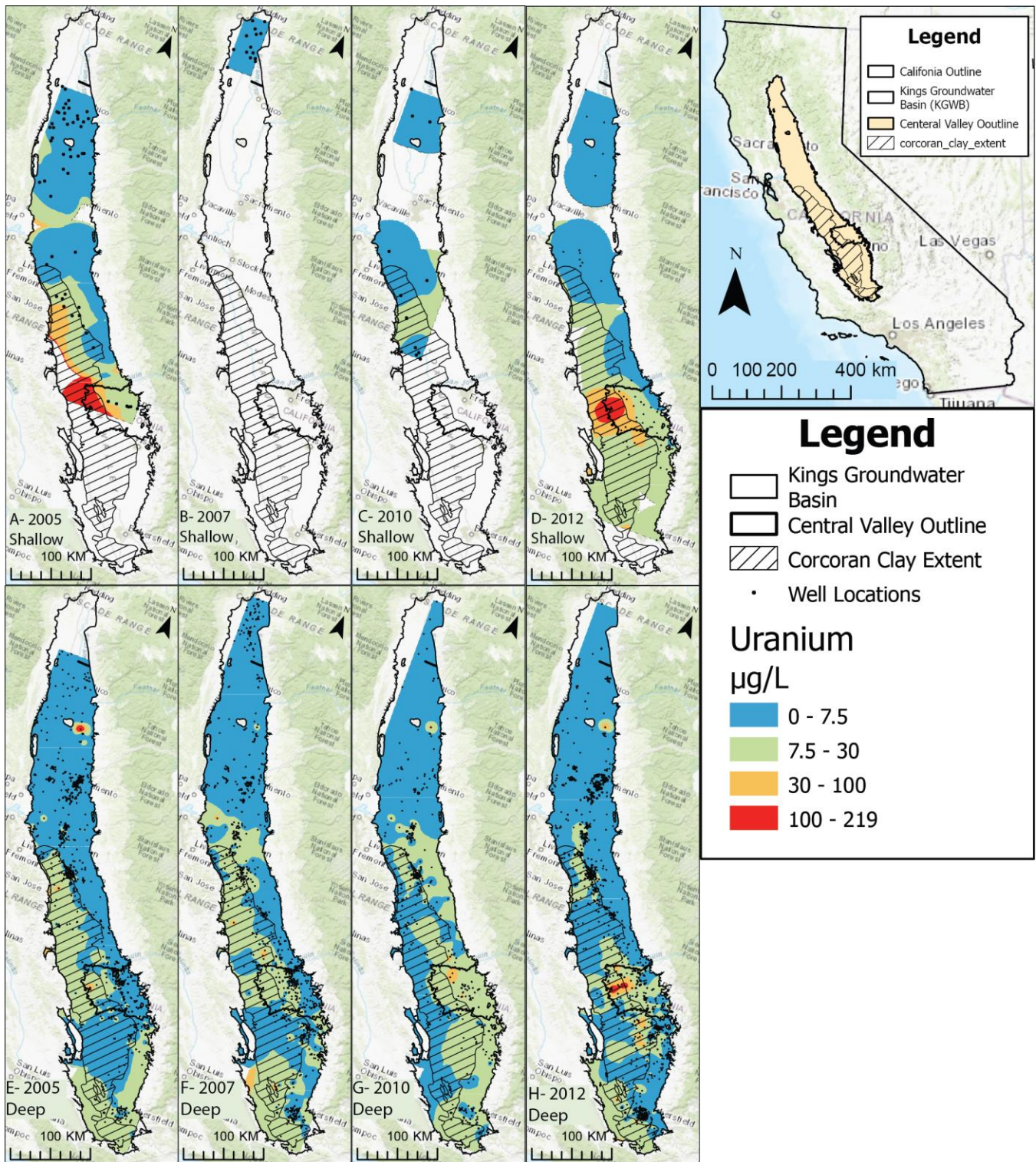
Figure 10. Spatial analysis showing U concentrations in the CV by coloration contours. Locations where well data was known are indicated by black dots, and the extent of the Corcoran Clay is cross hatched.
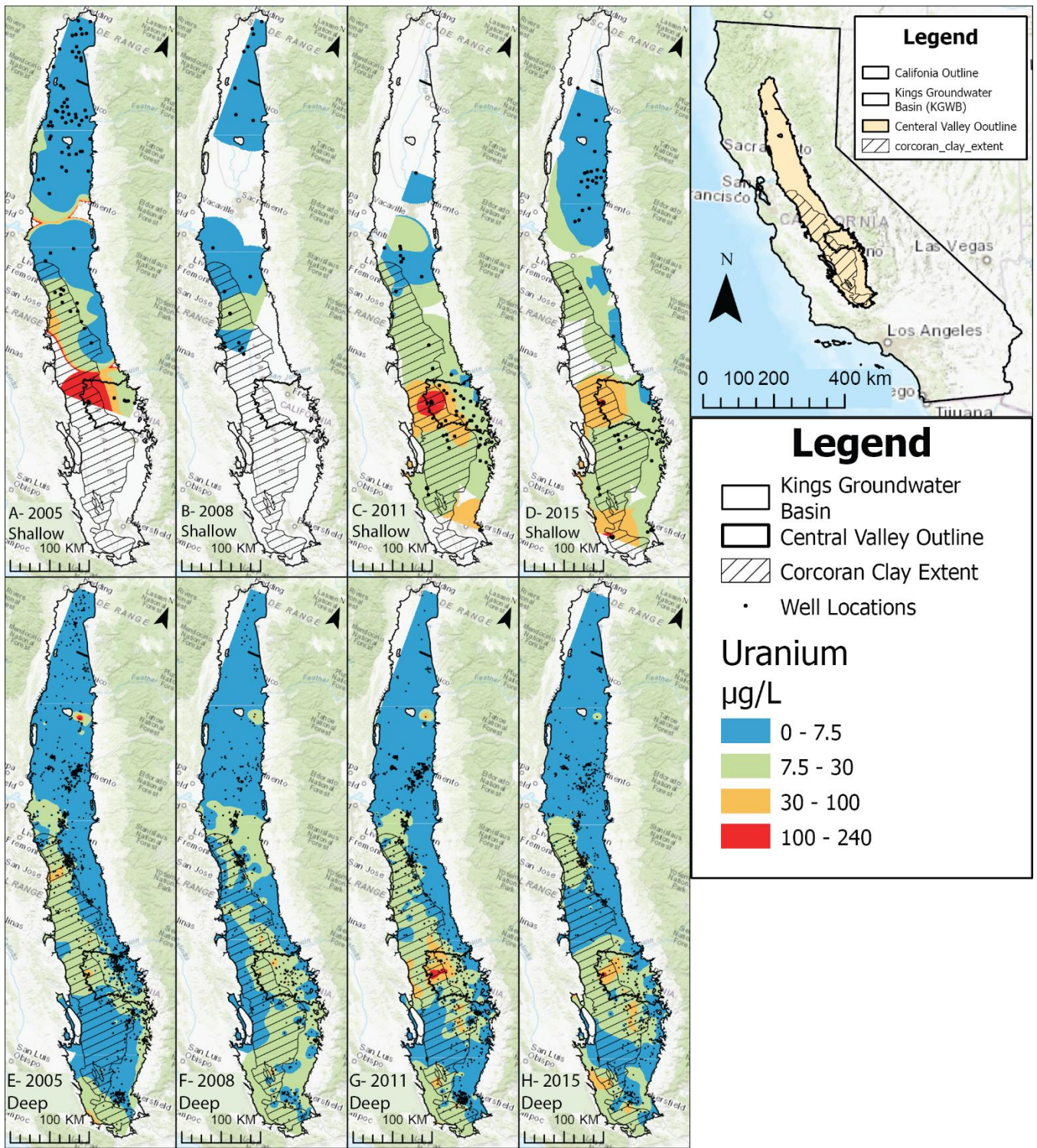
Figure 11. *Spatial analysis showing U concentrations in the CV by coloration contours in the wetting drying cycle. Locations where well data was known are indicated by black dots, and the extent of the Corcoran Clay is cross hatched.*

4.2.3.2 Uranium KGWB Observations

Uranium contamination in the CV was significant only in the KGWB in the central region of the CV (Figure 10 and 11). Therefore, I limited all further modeling of U and its mobilization mechanisms to the KGWB. For this detailed analysis, the time range was limited to a single snapshot in time, the 2012-2017 drought period.

4.2.3.2a Groundwater constituents
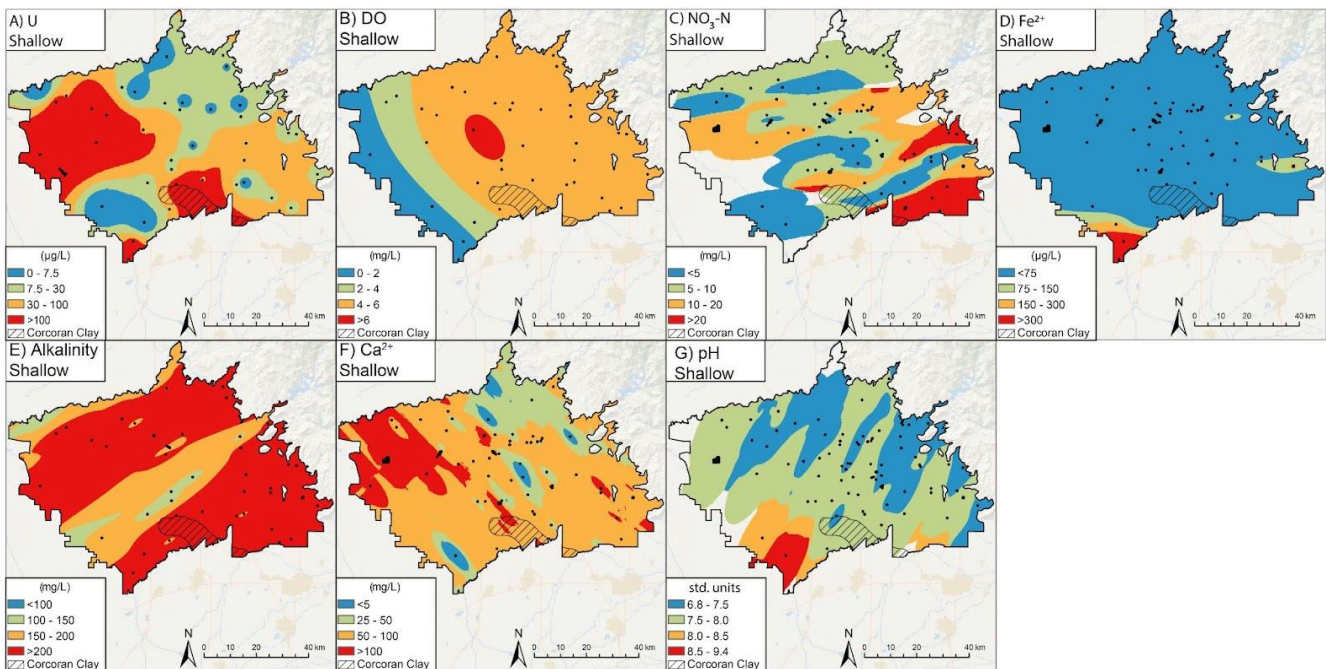
Figure 12. Kriged concentration maps for shallow groundwater in the Kings Groundwater Basin for A) U (µg/L), B) DO (mg/L), C) NO3-N (mg/L), D) Fe^{2+} (µg/L), E) alkalinity (mg/L as HCO$_3^-$), and G) pH. Dots indicate the well location used to inform the maps. Hatching indicates the extent of the Corcoran Clay at depths characterized as "shallow".

To investigate the spatial distribution of various geochemical mechanisms responsible for U in groundwater, I kriged concentration maps for several parameters (D.O., NO$_3^-$, Fe^{2+}, alkalinity, Ca^{2+}, pH and U) as shown in Figures 12 and 13. I considered D.O. and NO$_3^-$ because they are the primary electron acceptors that may oxidize U (Eqs 3 and 4). Fe^{2+} was included because U adsorbed to Fe hydroxides can be mobilized into groundwater due to Fe-reduction. Alkalinity and Ca^{2+} were included to assess the influence of (calcium)-uranyl-carbonate complexation (Eq. 5-9).

Lastly, pH was included as it influences numerous geochemical processes (mineral surface charge, carbonate equilibria, aqueous complex stability, etc.). It is important to note that there is a change in the depth that splits shallow and deep groundwater when using only the wells from the KGWB to define the splitting depth. This causes the U hotspot in deep groundwater from the CV (where the depth separating shallow from deep groundwater was 60 m below land surface) to now appear in shallow groundwater in the KGWB (where the depth separating shallow from deep groundwater as 74.7 m below land surface). In the shallow aquifer direct well measurement data U exceeds the MCL in 38% of the wells sampled in the KGWB. Furthermore, 55% of the wells exceeds half of the MCL, indicating widespread U contamination. Spatial interpolation of the shallow KGWB suggests that 58% of groundwater exceeds the MCL and 80% exceeds half of the MCL (Figures 12 and 13).

In the shallow aquifer of the KGWB, there are U concentrations exceeding the MCL (Figure 12A) in three regional hotspots. The largest of the three hotspots is located in the western region of the basin with a smaller region in the south-central KGWB, and a third small region in the far southern tip of the basin. D.O. is highest in the center of the KGWB and decreases radially, with the steepest concentration gradient toward the west (Figure 12B). Aquifer conditions are generally oxic (> 4 mg/L) except for the eastern region. Nitrate has inconsistent trends with high concentrations in the east of the basin and in the west roughly correlated with the U hotspot (Figure 12C). Fe^{2+} concentrations are generally low with the exception of the southern tip of the basin where groundwater is iron reducing ($Fe^{2+} > 300$ μg/L) (Figure 12D). Alkalinity is high throughout the entire basin, with especially high concentrations (> 200 mg/L) along two southwest-northeast trending strips with a region of lower concentration (< 200 mg/L) separating them (Figure 12E). Ca^{2+} is highest in the western region of the basin (> 100 mg/L), yet present throughout the majority

of the basin (Figure 12F). Lastly, pH in the basin is generally between 6.8 and 8 with the exception

of the southernmost tip, spatially correlated with both the higher levels of Fe^{2+} and one well with

elevated U (Figure 12G).
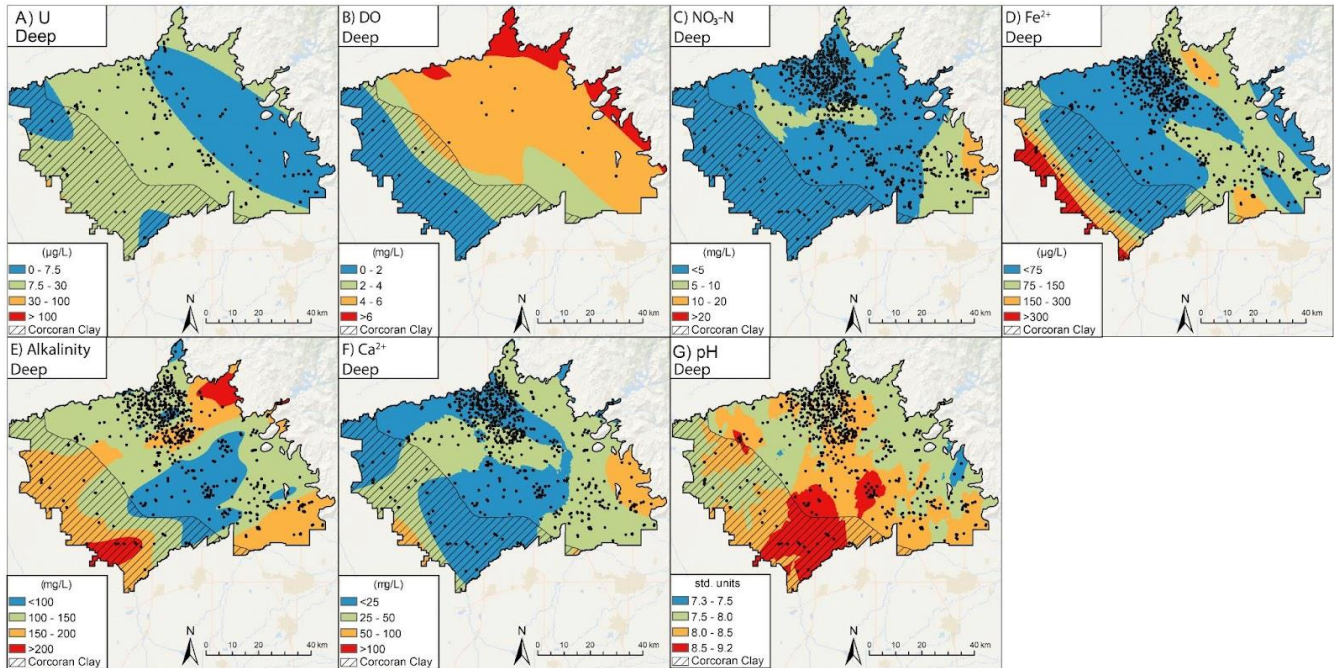
Figure 13. *Kriged concentration maps for deep groundwater in the Kings Groundwater Basin for A) U (µg/L), B) DO (mg/L), C) NO3-N (mg/L), D) Fe^{2+} (µg/L), E) alkalinity (mg/L as HCO_3^-), and G) pH. Dots indicate well location used to inform the maps. Hatching indicates the extent of the Corcoran Clay at depths charcterised as "deep".*

Geochemical maps for the deep aquifer are shown in Figure 13. Generally, groundwater

contamination by the species I considered is much lower in the deep groundwater compared to

shallow groundwater, although there is a trend of chemicals associated with more oxidizing

environments (D.O., NO_3^- , U in the east and chemicals associated with a more reducing

environment in the west (Fe^{2+}) (Figure 13). In the basin, U is generally less than the MCL of 30

µg/L, with a region < 7.5 µg/L on the eastern side that strikes from northwest to southeast. D.O. is

highest (> 6 mg/L) in the northeast and decreases toward the south and west (Figure 13A and B).

NO_3^- is highest in the far east of the basin, but it never exceeds 20 mg/L NO_3-N (Figure 12C). Fe^{2+}

is the highest in the far west of the basin, under the Corcoran Clay (Figure 13D). The kriged

interpretation suggests that concentrations of Fe^{2+} will exceed 300 µg/L in the far east, although there is both a lack of Fe^{2+} data in this region and the kriging algorithm is sensitive to increased uncertainty at the extremes of the study area that likely exaggerate Fe^{2+} concentrations. Alkalinity is significantly lower in deep groundwater than in the shallow aquifer, with a region below 100 mg/L in the center of the basin and two smaller regions above 200 mg/L in the northern and southern parts of the basin (Figure 13E). Ca^{2+} is generally below 50 mg/L with the exception of a small region in the far east (Figure 13F). Lastly, pH is higher than the shallow aquifer with nearly the whole basin greater than 7.5 and a large region in the south-central part of the basin greater than 8.5 (Figure 13G).

4.2.3.2b Spatial Correlation

Using concentrations from the spatial maps (250 x 250 m grid cells), I created spatial correlation maps (Figure 14) between U and the other species modeled in the shallow KGWB groundwater using Equations 5-9. Areas mapped for correlation only consider regions where U was > 1/4 of the MCL (> 7.5 µg/L). The U hotspot in the shallow aquifer in the western region of the KGWB is not correlated with D.O. whereas the U and D.O. are correlated in the south-central region. U and NO_3^- in shallow groundwater have a moderate-to-high correlation throughout the basin with especially high correlation in the south-central region. South of that hotspot the southernmost region of U contamination shows low correlation, although there is a lack of nitrate data which limits the confidence of that correlation. U-Fe^{2+} correlation is generally low throughout the KGWB with the exception of the southernmost region of elevated U where the correlation is high. Alkalinity has a moderate-to-high correlation with U throughout the basin, although its correlation is generally lower in the western hotspot. U-Ca^{2+} correlation is inconsistent. While there is some noise in the Ca^{2+} interpolation, there is a high correlation in the western U hotspot

with lower correlation elsewhere. pH has a low correlation in the two major U hotspots, while the southern hotspot shows moderate-to-high correlation.

U concentrations are low in the deep aquifer, so correlations were not explored as U mobilization is not occurring in appreciable amounts.
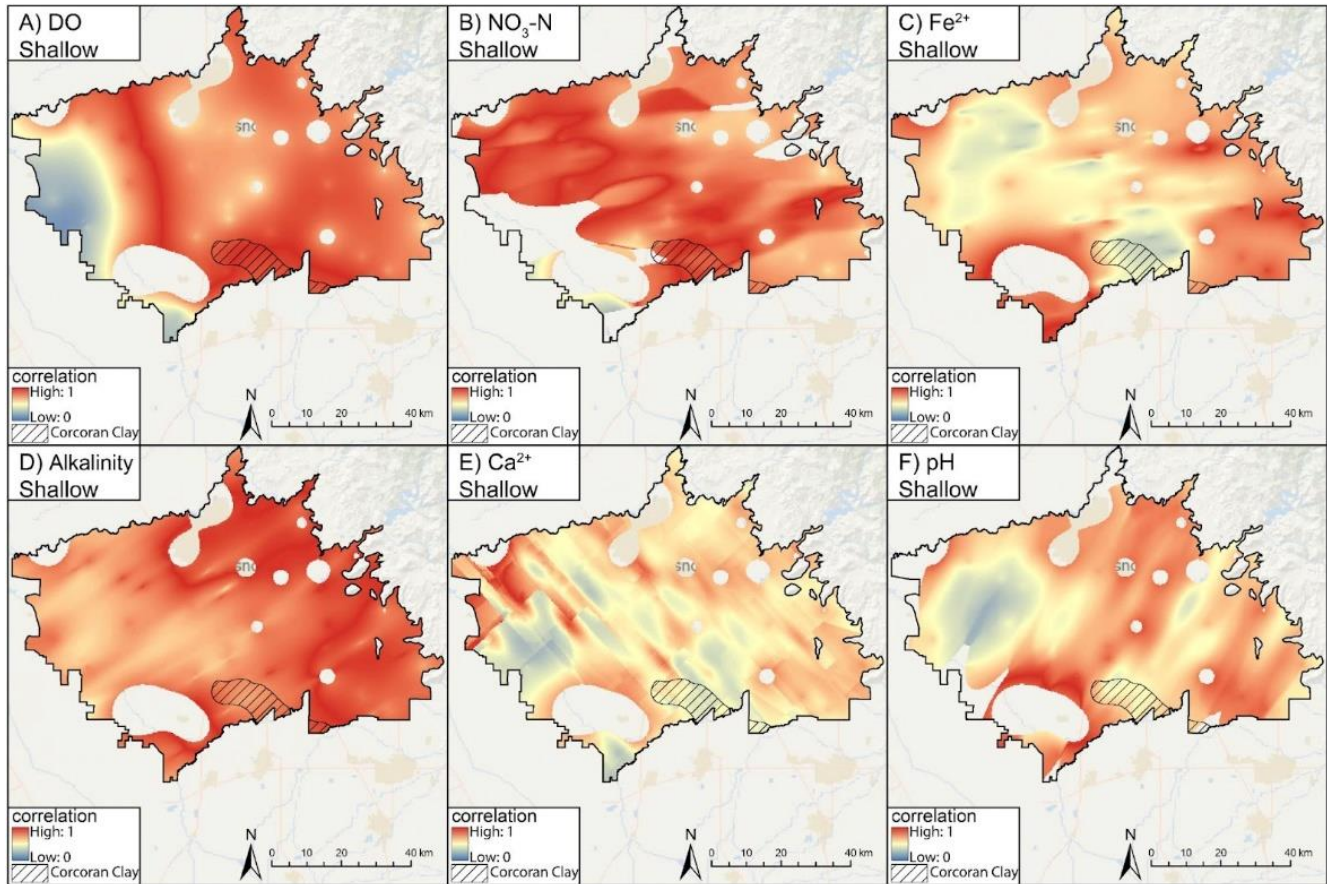
Figure 14. *Spatial correlation of U with A) DO, B) NO3-N, C) Fe^{2+}, D) alkalinity, E) Ca^{2+}, and F) pH in shallow groundwater in the KGWB. Hatching indicates the extent of the Corcoran Clay at shallow depths. For raster cells where U is <7.5 µg/L, no correlation value is displayed.*

4.2.3.2c Spatial Complexation

To quantify the spatial variation in uranyl carbonate and calcium-uranyl-carbonate complexation, I developed a spatial geochemical complexation analysis following the complexation reactions introduced before (Eqs. 5-9). Concentrations of UO_2^{2+}, $UO_2CO_3^0$, $UO_2(CO_3)_2^{2-}$, $UO_2(CO_3)_3^{4-}$,

$CaUO_2(CO_3)_3^{2-}$, $Ca_2UO_2(CO_3)_3^0$ ranged from 10^{-24} to 10^{-6} molal. Any value less than 10^{-8} molal was considered to be insignificant as it represented less than 1% of the total U concentration. UO_2^{2+} had no significant concentration and $UO_2CO_3^0$ only had one small section considered significant ($> 10^{-8}$ molal) which was located within the western hotspot (Figure 15 and 16).
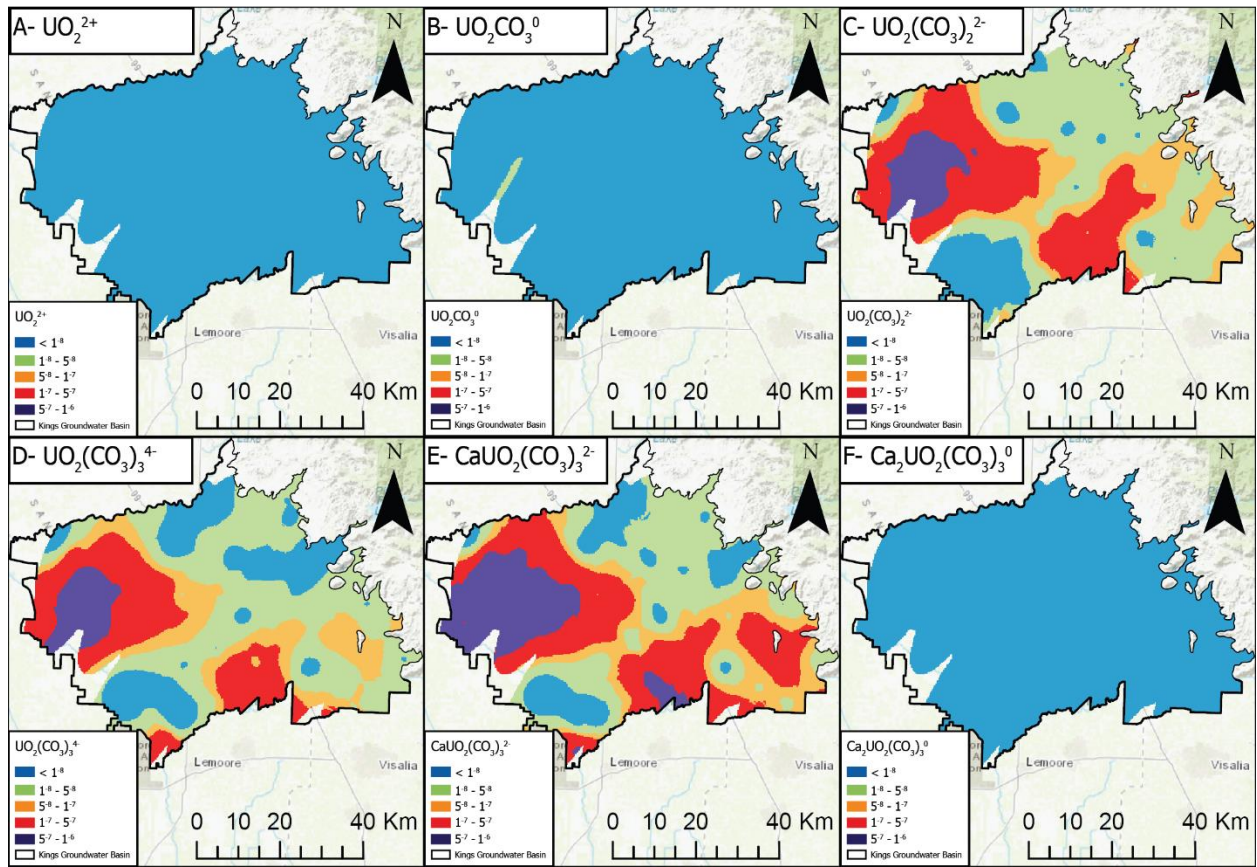
Figure 15. *Spatial complexation maps showing the modeled molality of each complex (A-F) which are the products of Eqs. 5-9.*

The concentration of $UO_2(CO_3)_2^{2-}$ was in excess of 10^{-6} molal and constituted up to 40% of the total dissolved U in the western hotspot. Slightly lower concentrations (1 to 5 x 10^{-7} molal) were present in the south-central hotspot as well, constituting 30% of total U in this region, although it is important to point out that the total U concentration was lower than in the western hotspot (Figure 15 and 16). $UO_2(CO_3)_3^{4-}$ has similar trends to $UO_2(CO_3)_2^{2-}$ with the highest levels present in the west which contribute ~20% of the total U in the region. $UO_2(CO_3)_3^{4-}$ represents less of the

south-central hotspot. However, it is still around 20% of the total (Figure 15 and 16). $UO_2(CO_3)_3^{4-}$ is the dominant species in the most southern hotspot. $CaUO_2(CO_3)_3^{2-}$ was higher than 10^{-6} molal in all three hotspots and had concentrations that were considered significant ($> 10^{-8}$ molal) across nearly the whole region. This species constituted up to 65% of the western hotpot, 50% of the south-central, and 20% of the most southern hotspot. Lastly, $Ca_2UO_2(CO_3)_3$ had no significant values throughout the basin. The deep aquifer does not have significant U contamination, and thus geochemical modeling was not performed.
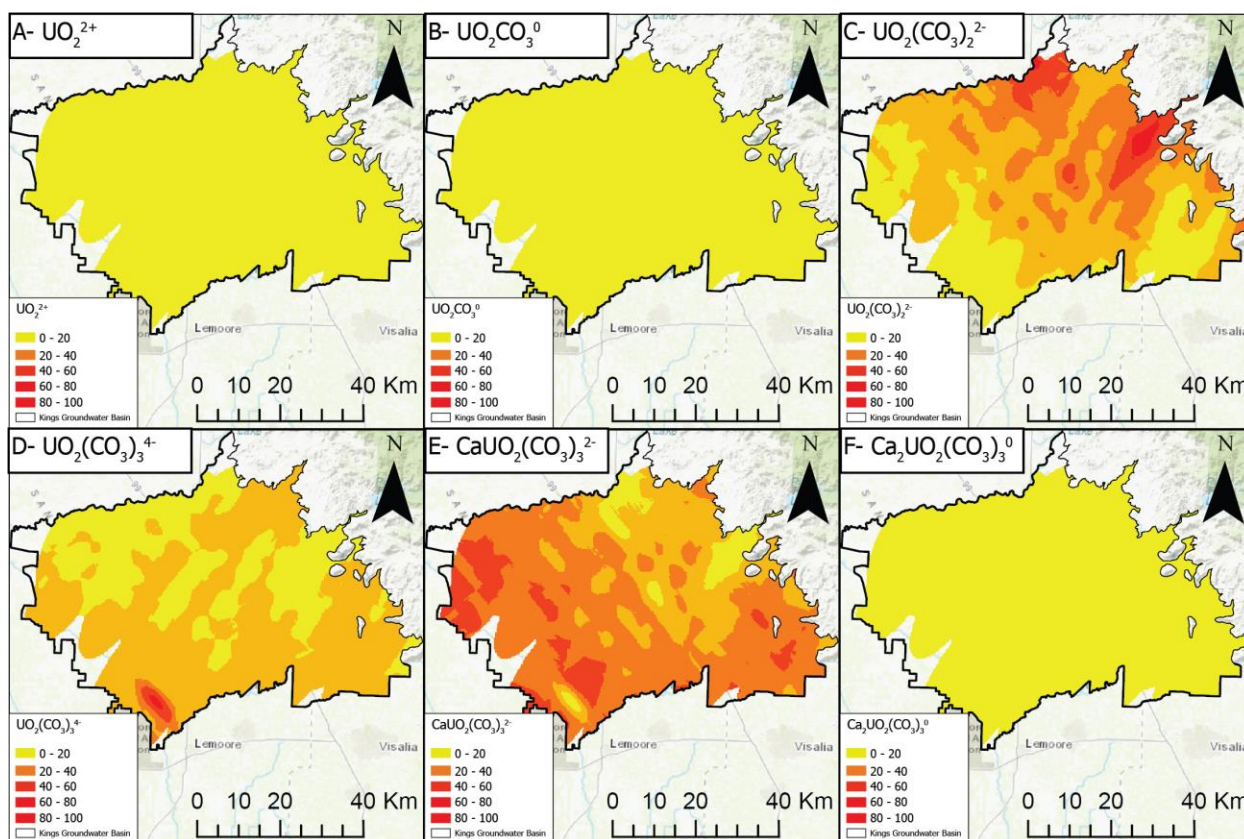
Figure 16. *Spatial complexation maps showing the precent abundance of each complex in a given cell relative to the total amount of U present in the cell.*

5. Discussion

5.1 Major Controls on Groundwater Quality in the CV

The PCA can be used to interpret the dominant controls on groundwater chemistry in the CV. In the positive PC1 dimension, there is a plethora of parameters. Most parallel to the PC1 axis were Na^+, Cl^-, T.D.S., and S.C. which along with other species in the positive direction are both charged and occur at high concentrations in groundwater. For PC1, which exerts the greatest control on CV-wide chemistry, there was a lack of vectors in the negative PC1 dimension, with the exception of D.O., which is an uncharged molecule. PC1 is likely related to the overall ionic strength of a groundwater sample, with ion-abundant groundwater samples receiving positive PC1 values and ion-poor samples receiving negative values. Furthermore, S.C., which is one of the two closest vectors to PC1 is a measure of the electric conductivity of water, which is directly related to the number of ions in solution (ionic strength). Additionally, because D.O. is associated with negative PC1 values, PC1 might also be related to groundwater age by reflecting the extent of water-rock interactions, with older water containing more ions from longer reactivity with soluble minerals and newer recharge water being comparatively ion poor with more D.O.. The Westside and Tracy/Delta-Mendota in the west have a high ionic strength, perhaps as a result of weathering of the marine sediments from the Coastal Range which are primarily carbonate and siliciclastic. Weathering of these rocks results in a relatively large number of dissolved ions released into the surrounding groundwater when compared to sediments derived from the granitic Sierra Nevada range. In contrast, the Redding region has water with relatively low ionic strength and is likely characterized by aquifer recharge. From the PCA it can also be inferred that Redding has the lowest degree of contamination of the CV, which is supported by spatial analysis (Figures 5, 6, 7, 9, 10, 11).

While PC2 explains less variability in the overall dataset, it is important for assessing As and U mobility. The juxtaposition between the cluster of NO_3^-, D.O., and H^+, versus the cluster of As, Fe^{2+}, and Mn^{2+} suggests PC2 relates to redox potential. The strong control of electron acceptors (D.O. and NO_3^-), which facilitate oxidation and reflect relatively oxygenated water, directly contrasts with three parameters (As, Fe^{2+}, and Mn^{2+}) generally mobilized through anaerobic redox reactions. The PCA suggests that As is related to Fe^{2+} and Mn^{2+} because of the relative proximity of their vectors and that it should generally be found in reducing groundwater. This interpretation is strengthened by the vector of well depth, which clusters near the reductively dissolved metals, suggesting that deeper waters will generally be more anoxic and contain As. Textural classes do not appear to be controlled by PC2 because the textural clusters tend to span a wide range of positive and negative values in the PC2 dimension. However, this makes sense because each region had data from both the shallow and deep aquifers, and generally the shallow aquifers are more oxic and ion-poor while the deeper aquifers are more anoxic and ion-rich. Because the U vector occurs in the positive PC1 and PC2 dimension, its presence is likely influenced by both high ionic strength, which likely influences complexation via alkalinity and Ca^{2+}, and oxidizing conditions, which facilitates oxidative dissolution from uraninite (Eqs. 3-9).

5.2 Arsenic Mobilization

5.2.1 Geochemistry of Arsenic Mobilization

In the CV, As mobilization appears closely related to reduction of iron and/or manganese oxides. Statistically, the closest related variables to As are Fe^{2+}, Mn^{2+} and well depth (Figure 3). It has been reported in the literature that As adsorbs strongly to positively charged surfaces of Fe and Mn oxides (Fendorf et al., 2010; McKenzie, 1981; Pierce and Moore, 1982; Stahl and James, 1991). If Fe^{2+} is reductively dissolved, as is suggested by the statistical analysis, any ion attached

to the surface will be introduced into groundwater as well as the Fe^{2+} or Mn^{2+} from the mineral surface site itself. Given that the spatial analysis indicates that As tends to only exist in groundwater if Fe^{2+} and Mn^{2+} are also present, reductive dissolution is likely the dominant mechanism for As in groundwater throughout the CV in both the shallow aquifer and SV deep hotspot. The deep aquifer SJV hotspot seems to be solely related to the Corcoran Clay rather than Fe^{2+} dissolution, as Figure 6 shows a limited presence of Fe^{2+} in the SJV where As concentrations are high.

The relationship of well depth and As also likely relates to elevated Fe^{2+} and Mn^{2+}. Generally, the most favorable electron acceptors in groundwater systems originate at earth's surface (D.O. from the atmosphere and NO_3^-, often from agriculture). Because they are thermodynamically favorable, they are consumed earliest along a groundwater flow path (i.e., generally in shallower waters and along valley recharge), giving way to deeper aquifer environments becoming anoxic and reductively dissolving Fe^{2+} and Mn^{2+} oxides. In the SJV, the eastern edge where the Corcoran Clay is absent, D.O. and NO_3^- infiltrate downward with recharge water creating oxic conditions, thus explaining the lack of As contamination.

5.2.2 Physical Influences on Arsenic Mobilization

In the SJV, there is a remarkable spatial overlap between regions of elevated As and the Corcoran Clay, which bisects the shallow and deep aquifers. The release of As from clay strata in the Corcoran Clay has been hypothesized previously (Fendorf et al., 2010.; Smith et al., 2018) both spatially and geochemically. Arsenic was weathered and transported from the Sierra Nevada by the rivers that fed a Holocene lake that deposited the Corcoran Clay, where As was then sorbed onto particles in the clay fraction in lake sediments. However, the specific mineralogy hosting As remains unclear. Gao et al. (2004) identified As in sediments containing mostly smectite,

montmorillonite, and kaolinite as the dominant mineralogy. However, given that these minerals do not generate positive surface charge, they are likely not the host of As oxyanions. Others have suggested that As tends to associate with hydroxides in the clay particle size fractions (Fendorf et al., 2010). Likely, over time the water in the pore space of the saturated clay became anoxic due to microbial metabolism of organic carbon, reducing Fe and Mn hydroxides and subsequently mobilizing the As that was sorbed to them, but the mobilized As was trapped in the pore water of the clay strata. However, the development of groundwater pumping in the region over the past 100 years has substantially altered the regional hydrogeology. Clays, which create a 'house of cards' morphology are compressed with a reduction in fluid pressure due to over pumping. As the clays compact to accommodate the loss of fluid pressure, clay pore space is lost, and pore water is released into the surrounding aquifer. It has also been shown that over pumping has lowered the potentiometric surface of the deep confined aquifer below the water table in the overlying shallow aquifer, resulting in a downward vertical gradient, rather than the primarily horizontal gradient that is present with an unperturbed aquifer (Smith et al., 2018). The significance of this change is demonstrated in the decrease in shallow SJV As conditions demonstrated in this study, while As-rich pore water from the clay is hydraulically drawn downward into deep groundwater.

Because the Corcoran Clay is constrained to the SJV, the As hotspot in the SV likely is attributable to a different phenomenon. Spatially, the area with high As in the SV is proximal to Sutter Buttes (the small region of volcanics in the CV (Figure 1)). Sutter Buttes is an inactive intermediate volcano whose rocks serve as the source material for much of the sediment in its vicinity. Weathering of sulfate-bearing volcanics, and specifically volcaniclastics, can lead to the mobilization of As (Kim et al., 2011). Such volcaniclastics have been suggested to be present in the Sutter Buttes area as the volcano is weathered, specifically in the ramparts surrounding the

dome. It is hypothesized that those ramparts could be a source of the elevated levels of As in the SV (Springhorn, 2008). While Springhorn (2008) showed a correlation between rampart volcaniclastics and As concentrations, a detailed geochemical analysis is necessary to elucidate the mobilization mechanism. While the relationship between rampart volcaniclastics could explain the persistent As concentrations in the deep aquifer, it fails to explain why the contamination appears to not be present in 2005-2007 and 2007-2009 in the shallow aquifer.

5.2.3 Climactic Influences on Arsenic Mobilization

One of the clearest differences between the shallow and deep aquifers was in stability of As concentrations during periods of climactic change. The shallow aquifer seemed to change in spatial extent and magnitude of As contamination in every time period in both the SV and SJV. In the interpolation process, I found that errors were high, which suggests a relatively high amount of variation within the given time period and aquifer. This may be due to climactic variation and its influence on shallow groundwater. Because As concentrations are sensitive to pH and redox conditions, a rapid influx of meteoric water with high D.O. and low pH likely promotes oxidizing conditions and generates stable sorbed As to iron hydroxides, as lower pH water enhances generation of positive hydroxide surfaces that promote sorption of As oxyanions. This hypothesis is supported in the spatial analysis where conditions improve from the drought of 2007-2010 to the non-drought of 2010-2012 (Figure 4B-C) and furthermore in the PCA (Figure 3) where dissolved As is juxtaposed with H^+. Furthermore, large rainfall events likely flush NO_3^- stored in the unsaturated zone during drought periods into groundwater, introducing an electron acceptor that further staves off anoxia, and thus As mobilization. Conversely, if rainfall is limited due to drought, the concentration of NO_3^- in the unsaturated zone will build up until the drought ends.

Without recharge, NO_3^- and D.O. do not replenish an aquifer, driving groundwater to more anoxic conditions which favor As mobility.

In contrast to the shallow aquifer, As in the deep aquifer was consistent over time both in terms of the magnitude and spatial extent. Arsenic contamination was consistently proximal to the Corcoran Clay in the SJV and to Sutter Buttes in the SV. A lack of climactic influence highlights that deeper groundwater is more stable over time and is less susceptible to changes occurring on earth's surface, at least over the decadal timescale.

5.3 Uranium Mobilization

5.3.1 Geochemistry of Uranium Mobilization

The position of the U vector in the groundwater PCA (Figure 3) suggests that U is found in oxidizing conditions. U occurs naturally in the mineral uraninite in mafic and ultramafic rocks, which are present in the igneous Sierra Nevada (shown in purple in Figure 1) that supplies the sediment for the CV. In sediment, U can be can be mobilized from uraninite via oxidation caused by either D.O. or NO_3^- (Eqs. 3 and 4). Oxidation by D.O. is the most thermodynamically preferred pathway, thus should uraninite be in the presence of D.O., the reaction shown in Equation 3 would take place. However, spatial analysis shows that U typically is not abundant in high concentration in the presence of D.O., likely due to some combination of three reasons: 1) D.O. is only supplied via recharge and is saturated in water at relatively low concentrations (~8 to 10 mg/L, depending on temperature), so it cannot accumulate to high concentrations to cause substantial U mobilization; 2) U oxidation occurs in the vadose zone, where pore space is unsaturated, limiting the mass of D.O. available for oxidation compared to phreatic sediments; and 3) D.O. is likely consumed due to high chemical oxygen demand in more thermodynamically (bio)geochemical reactions, such as oxidation of organic carbon (logK often $> 10^{100}$) facilitated by microorganisms,

further minimizing the amount of D.O. available for uraninite oxidation. In contrast, NO_3^- is prevalent throughout the shallow KGWB due to widespread application of NO_3^--bearing fertilizer used in agriculture. When U is mobilized in the presence of NO_3^-, U accumulates to much higher concentrations than when it is in the presence of D.O.. This is likely because NO_3^- is highly soluble and is not saturation-limited at low concentrations like D.O..

Additionally, statistical trends of U in groundwater of the CV show that U clusters most closely to alkalinity, Mg^{2+}, and Ca^{2+} (Figure 3). These results support a recent study by Lopez et al. (2021), who used random forest tree regression modeling to show that Ca^{2+} and Mg^{2+} were the best predictors of high U concentrations in the CV. The explanation of why Ca^{2+} and Mg^{2+} are good predictors of U concentrations are the complexation Equations 5-9 from Dong and Brooks (2006).

Elevated levels of these ions can stabilize U via formation of calcium uranyl carbonate complexes. My geochemical modeling suggested that these phases were important contributors to elevated U in groundwater. For the western hotspot, the dominant species was $CaUO_2(CO_3)_3^{2-}$, contributing 65% of the total U in groundwater. In the south-central hotspot $CaUO_2(CO_3)_3^{2-}$ contributed 50% of the total U concentration, with $UO_2(CO_3)_2^{2-}$ and $UO_2(CO_3)_3^{4-}$ splitting the remaining 50% roughly evenly. Combined, these phenomena suggest that oxidation by nitrate likely serves as the main trigger for U mobilization. However, U can be stabilized in groundwater via the formation of calcium uranyl carbonate complexes. In fact, U typically only accumulates to high concentrations in groundwater when these complexes are dominant. One exception to this is in the localized southern hotspot, where $UO_2(CO_3)_3^{4-}$ was the dominant U species Thus, in the three areas with elevated levels of U, complexation was involved with no significant levels of UO_2^{2+} present anywhere in the basin.

5.3.2 Physical Influences on Uranium Mobilization

The predominant physical influence in the KGWB, a subsection of the SJV, is the Corcoran Clay. The Corcoran Clay facilitates the establishment of anoxic conditions by inhibiting recharge of oxygenated water in the deep confined aquifer. U is present under oxidizing conditions, thus the deeper, older, and more anoxic groundwater (like that confined below the Corcoran Clay) should be free of significant U contamination. I found this to be true in my spatial analysis (Figures 10 and 11). Land use change and intensification of agriculture likely impacts U mobility. U mobilization could be accelerated due to the elevated NO_3^- used as fertilizer, and due to excess CO2 in vadose zone soils from crop respiration. Plants introduce CO_2 into the soil which reacts with soil pore water to produce carbonic acid. The impact of this introduction of carbonic acid is twofold: 1) when carbonic acid deprotonates into either bicarbonate or carbonate (depending on pH conditions) it can facilitate the complexation modeled in section 4.2.4.2c (Langmuir, 1997); 2) acidification of groundwater favors calcite dissolution which would increase aqueous Ca^{2+}, again furthering the complexation of U (Dong and Brooks, 2006; Lopez et al., 2021). Both of these complexation reactions inhibit the ability of U to reassociate with sediment phases, enhancing U solubility.

5.3.3 Climactic Influences on Uranium Mobilization

In the CV, drought/non-drought is the dominant climactic cycle. Drought minimizes the infiltration of both D.O. and NO_3^- into the aquifer. In a period of drought with limited recharge, new oxic and NO_3^--bearing water does not reach the phreatic zone to provide the electron acceptors that can trigger redox reactions, likely driving the aquifer as a whole to more reducing conditions. Because of this, any U that is present will likely remain in the mineral due to a lack of electron-acceptors to facilitate its oxidation. Meanwhile, NO_3^- from fertilizer can be stored in the

unsaturated zone at high concentrations. However, at the start of a non-drought period, an influx of recharge water rich in D.O. and NO_3^- can trigger U mobilization and carry U into groundwater to potentially unsafe concentrations.

6. Conclusions

U and As are both inorganic geogenic contaminants that have been mobilized in the CV of California, threatening the primary water source for millions of people and billions of dollars in industry. Here, I have investigated the mobilization of those geogenic contaminants and the human impact on those contaminant pathways.

The release of As in the CV in the southern SJV spatially correlates to the Corcoran Clay and likely occurs because of dewatering of the Corcoran Clay unit due to over-pumping and clay compression. In the northern SV, there appears to be multiple factors contributing to the release of As, including the weathering of volcaniclastics from Sutter Buttes. In both locations, As is chemically linked to Fe^{2+} and/or Mn^{2+}, suggesting that As initially is sorbed to Fe and/or Mn oxides that are reductively dissolved due to microbial activity. If groundwater withdrawals are not limited as climate change intensifies drought conditions, As contamination will likely continue to increase in both extent and intensity.

U occurs in uraninite in mafic sediments and appears to be mobilized and stabilized by a multi-step chemical process. While D.O. can oxidatively dissolve U, the presence of NO_3^- appears to be key to high U concentrations in groundwater. The subsequent UO_2^{2+} ion then reacts with the surrounding CO_3^{2-} and Ca^{2+} to form aqueous complexes that can stabilize the complex in groundwater. The primary anthropogenic driver of U mobilization is agriculture, which is intense throughout the CV impacting both redox potential and stability of aqueous U complexes.

7. Acknowledgements

8. References

Abdelouas, A., 2006. Uranium Mill Tailings: Geochemistry, Mineralogy, and Environmental Impact. Elements 2, 335–341. https://doi.org/10.2113/GSELEMENTS.2.6.335

Burow, K.R., Jurgens, B.C., Belitz, K., Dubrovsky, N.M., 2013. Assessment of regional change in nitrate concentrations in groundwater in the Central Valley, California, USA, 1950s-2000s. Environ Earth Sci 69, 2609–2621. https://doi.org/10.1007/s12665-012-2082-4

Chappelle, C., Hanak, E., Harter, T., 2020. Groundwater in California.

Dong, W., Brooks, S.C., 2006. Determination of the formation constants of ternary complexes of uranyl and carbonate with alkaline earth metals (Mg2+, Ca2+, Sr 2+, and Ba2+) using anion exchange method. Environ Sci Technol 40, 4689–4695. https://doi.org/10.1021/es0606327

Famiglietti, J.S., Lo, M., Ho, S.L., Bethune, J., Anderson, K.J., Syed, T.H., Swenson, S.C., de Linage, C.R., Rodell, M., 2011. Satellites measure recent rates of groundwater depletion in California's Central Valley. Geophys Res Lett 38. https://doi.org/10.1029/2010GL046442

Faunt, C.C., Hanson, R.T., Belitz, K., Schmid, W., Predmore, S.P., Rewis, D.L., McPherson, K., 2009. Groundwater Availability of the Central Valley Aquifer, Califonia.

Faunt, C.C., Sneed, M., Traum, J., Brandt, J.T., 2016. Water availability and land subsidence in the Central Valley, California, USA. Hydrogeol J 24, 675–684. https://doi.org/10.1007/s10040-015-1339-x

Fendorf, S., Michael, H.A., Van Geen, A., 2010. Spatial and Temporal Variations of Groundwater Arsenic in South and Southeast Asia. Science (1979) 328, 1123–1127.

Fleckenstein, J., Anderson, M., Fogg, G., Mount, J., 2004. Managing Surface Water-Groundwater to Restore Fall Flows in the Cosumnes River. J Water Resour Plan Manag 130, 301–310. https://doi.org/10.1061/(asce)0733-9496(2004)130:4(301)

Frink, J.W., Kues, H.A., 1954. Corcoran Clay--A Pleistocene Lacustrine Deposit in San Joaquin Valley, California. Am Assoc Pet Geol Bull 38, 2357–2371. https://doi.org/10.1306/5ceae0a0-16bb-11d7-8645000102c1865d

Gao, S., Fujii, R., Chalmers, A.T., Tanji, K.K., 2004. Evaluation of Adsorbed Arsenic and Potential Contribution to Shallow Groundwater in Tulare Lake Bed Area, Tulare Basin, California. Soil Science Society of America Journal 68, 89–95. https://doi.org/10.2136/SSSAJ2004.8900

Ghasemizade, M., Asante, K.O., Petersen, C., Kocis, T., Dahlke, H.E., Harter, T., 2019. An Integrated Approach Toward Sustainability via Groundwater Banking in the Southern Central Valley, California. Water Resour Res 55, 2742–2759. https://doi.org/10.1029/2018WR024069

Guo, X., Chen, R., Liu, Q., Liu, J., Zhang, H., Yu, J., Li, R., Zhang, M., Wang, J., 2018. Superhydrophilic phosphate and amide functionalized magnetic adsorbent: a new combination of anti-biofouling and uranium extraction from seawater. Environ Sci Nano 5, 2346–2356. https://doi.org/10.1039/C8EN00545A

He, M., Russo, M., Anderson, M., 2017. Hydroclimatic Characteristics of the 2012–2015 California Drought from an Operational Perspective. Climate 2017, Vol. 5, Page 5 5, 5. https://doi.org/10.3390/CLI5010005

Jakhu, R., Mehra, R., Mittal, H.M., 2016. Exposure assessment of natural uranium from drinking water. Environ Sci Process Impacts 18, 1540–1549. https://doi.org/10.1039/C6EM00514D

Kim, D., Miranda, M.L., Tootoo, J., Bradley, P., Gelfand, A.E., 2011. Spatial Modeling for Groundwater Arsenic Levels in North Carolina. Environ. Sci. Technol 45, 4824–4831. https://doi.org/10.1021/es103336s

Krivoruchko, K., Gribov, A., 2019. Evaluation of empirical Bayesian kriging. Spat Stat 32. https://doi.org/10.1016/J.SPASTA.2019.100368

Langmuir, D., 1997. Aqueous Environmental Geochemistry by Langmuir, Donald: Good (1997) | Zoom Books Company [WWW Document]. Aqueous Environmental Geochemistry. URL https://www.abebooks.com/servlet/BookDetailsPL?bi=31428095978&searchurl=isbn%3D9 780023674129%26sortby%3D17&cm_sp=snippet-_-srp1-_-title1 (accessed 4.4.23).

Levy, Z.F., Jurgens, B.C., Burow, K.R., Voss, S.A., 2021. Critical Aquifer Overdraft Accelerates Degradation of Groundwater Quality in California ' s Central Valley During Drought Geophysical Research Letters 1–10. https://doi.org/10.1029/2021GL094398

Lopez, A.M., Wells, A., Fendorf, S., 2021. Soil and Aquifer Properties Combine as Predictors of Groundwater Uranium Concentrations within the Central Valley, California. Environ Sci Technol 55, 352–361. https://doi.org/10.1021/ACS.EST.0C05591/ASSET/IMAGES/LARGE/ES0C05591_0005.J PEG

McKenzie, R.M., 1981. The surface charge on manganese dioxides. Soil Research 19, 41–50. https://doi.org/10.1071/SR9810041

Nelson, T., Chou, H., Zikalala, P., Lund, J., Hui, R., Medellín-Azuara, J., 2016. Economic and water supply effects of ending groundwater overdraft in California's Central Valley. San Francisco Estuary and Watershed Science 14. https://doi.org/10.15447/sfews.2016v14iss1art7

Nolan, J., Weber, K.A., 2015. Natural Uranium Contamination in Major U.S. Aquifers Linked to Nitrate. https://doi.org/10.1021/acs.estlett.5b00174

Pavley, F., Dickinson, R., 2014. SB-1168 Groundwater management.

Pierce, M.L., Moore, C.B., 1982. Adsorption of arsenite and arsenate on amorphous iron hydroxide. Water Res 16, 1247–1253. https://doi.org/10.1016/0043-1354(82)90143-9

Podgorski, J., Berg, M., 2020. Global threat of arsenic in groundwater. Science (1979) 368, 845–850. https://doi.org/10.1126/science.aba1510

Reimann, C., Matschullat, J., Birke, M., Salminen, R., 2009. Arsenic distribution in the environment: The effects of scale. Applied Geochemistry. https://doi.org/10.1016/j.apgeochem.2009.03.013

Rosenblatt, M., 1956. Remarks on Some Nonparametric Estimates of a Density Function. https://doi.org/10.1214/aoms/1177728190 27, 832–837. https://doi.org/10.1214/AOMS/1177728190

Schmid, W., Hanson, R.T., Maddock Iii, T., Leake, S., Leake Hydrology, S.A., 2006. User guide for the Farm Process (FMP1) for the U.S. Geological Survey's modular three-dimensional finite-difference ground-water flow model, MODFLOW-2000 DFAT-CSIRO Indus SDIP Project View project Distinguishing Streamflow Depletion from Capture in a Semi-Arid Region View project.

Smith, R., Knight, R., Fendorf, S., 2018. Overpumping leads to California groundwater arsenic threat. Nat Commun 9, 1–6. https://doi.org/10.1038/s41467-018-04475-3

Springhorn, S.T., 2008. STRATIGRAPHIC ANALYSIS AND HYDROGEOLOGIC CHARACTERIZATION OF CENOZOIC STRATA IN THE SACRAMENTO VALLEY NEAR THE SUTTER (Masters). Califona State University, Sacramento.

Stahl, R.S., James, B.R., 1991. Zinc Sorption by Manganese-Oxide-Coated Sand as a Function of pH. Soil Science Society of America Journal 55, 1291–1294. https://doi.org/10.2136/SSSAJ1991.03615995005500050016X

Thiros, S.A., Paul, A.P., Bexfield, L.M., Anning, D.W., 2014. Water Quality in Basin-Fill Aquifers of the Southwestern United States: Arizona, California, Colorado, Nevada, New Mexico, and Utah, 1993–2009.

Voegtlin, C., Hodge, H., 1953. Uranium tetrachloride: Toxicity following inhalation for 1 and 2 years. McGraw-Hill Book Company, Inc , New York, NY .

Walton, G., 1951. Survey of Literature Relating to Infant Methemoglobinemia Due to Nitrate-Contaminated 'Water.

Wasserman, G.A., Liu, X., LoIacono, N.J., Kline, J., Factor-Litvak, P., Van Geen, A., Mey, J.L., Levy, D., Abramson, R., Schwartz, A., Graziano, J.H., 2014. A cross-sectional study of well water arsenic and child IQ in Maine schoolchildren. Environ Health 13. https://doi.org/10.1186/1476-069X-13-23

White, A.F., Peterson, M.L., Solbau, R.D., 1990. Measurement and Interpretation of Low Levels of Dissolved Oxygen in Ground Water. Groundwater 28, 584–590. https://doi.org/10.1111/J.1745-6584.1990.TB01715.X

Yoshida, T., Yamauchi, H., Fan Sun, G., 2004. Chronic health effects in people exposed to arsenic via the drinking water: dose–response relationships in review. Toxicol Appl Pharmacol 198, 243–252. https://doi.org/10.1016/J.TAAP.2003.10.022

Zheng, Z., Tokunaga, T.K., Wan, J., 2003. Influence of Calcium Carbonate on U(VI) Sorption to Soils. Environ Sci Technol 37, 5603–5608. https://doi.org/10.1021/ES0304897/SUPPL_FILE/ES0304897_S.PDF